Dakar Mosque gridshell: Exploring the benefits of the improved multibody rope approach through postbuckling analysis

# Dakar Mosque gridshell: exploring the benefits of the improved multibody rope approach through postbuckling analysis

Jonathan Melchiorre[a,*], Amedeo Manuello Bertetto[a], Stefano Invernizzi[a], Giuseppe Carlo Marano[a,b], Fabio Bazzucchi[a,c]

[a] *Politecnico di Torino, DISEG, Department of Structural, Geotechnical and Building Engineering, Corso Duca Degli Abruzzi, 24, Turin, 10129, Italy*
[b] *Fuzhou University, College of Civil Engineering, Xueyuan Rd, Gulou District, Fuzhou, 350025, China*
[c] *Senseable City Lab, Massachusetts Institute of Technology, Cambridge, MA., 77 Massachusetts Avenue, Cambridge, MA 02139, USA*

**Abstract**

This paper presents a comparative study of a gridshell roof structure designed for the Islamic Cultural Center in Dakar, Senegal. The structure, conceived by Fragomeli & Partners, emulates the shape of a dune to seamlessly integrate with the surrounding environment. To define an optimal structural shape while preserving the architectural intent, two form-finding methodologies were employed. The first method, the Multibody Rope Approach (MRA), enables the calculation of the funicular structural shape in response to the imposed load configuration. The second method, Improved MRA (i-MRA), introduces slight geometric variations to the funicular shape to reduce the diversity of structural elements required for construction. This work investigates the impact of the geometric distortions introduced by i-MRA on structural stability. Linear buckling modal analysis has been conducted on the two generated geometries, taking into account various loading conditions and structural element slenderness. Through incremental load Geometrical Non-linear with Imperfection Analyses (GNIAs) the equilibrium paths are examined to analyze the postbuckling behaviour of the gridshells. In the final step, the elastoplas-

*Corresponding author.
*Email address:* jonathan.melchiorre@polito.it (Jonathan Melchiorre)

tic constitutive law is incorporated to assess also the impact of material non-linearity. The models are examined through incremental load Geometrical and Material Non-linear Analyses (GMNIAs). The results indicate that the i-MRA geometry exhibits a more even stress distribution and better qualitative postbuckling behaviour.

*Keywords:* Gridshell, Multi-body Rope Approach, Postbuckling, Snap through instability, Nonlinear bifurcation

## 1. Introduction

Architecture and structural engineering are closely intertwined, with architecture influencing and being influenced by structural design. Over time, these disciplines have evolved hand in hand, responding to the ever-changing needs and aspirations of society. The dynamic relationship between architecture and structure has played a pivotal role in shaping a wide range of structural typologies and forms [1]. This holds in particular for the spatial structures in which the shape is strictly interconnected with the stress distribution. In this context, form-finding methodologies were introduced during the 1960s and 70s to establish the structural geometry as a function of the load field. These techniques have found extensive application, especially in the design of shells and gridshells [2]. Concerning structural stability, gridshells can be considered as single-layer reticulated shells. Architectural audacity and complexity require safety analyses for structural integrity beyond the standard procedures [3]. In this regard, the IASS (International Association for Spatial Structures) published comprehensive guidelines to buckling load evaluation of metal structures [4]. To incorporate all the non-univocal aspects behind buckling collapse, different analyses and approaches are indicated to assess the final design critical load. The elastic buckling load $Q_{EB}$

is usually evaluated through a Geometrically Nonlinear with Imperfection Analysis (GNIA) or Geometrically and Material Nonlinear with Imperfection Analysis (GMNIA). The loading patterns, and the related displacement coordinate $\delta_i$ for which to evaluate the equilibrium path, are selected through the the linear eigenvalue extraction for the $n$ design combination load factors $\Lambda_n$. The generic Euler load $Q_{CRi} = \Lambda_i q_i$, being $q_i$ the total applied load in the $i-th$ combination, and the maximum modal displacement are then used as a set parameters for the GNIAs. A linear static analysis of the structure loaded by $Q_{CR}$ provides the critical displacement $\delta_{CR}$, measured at the maximum node displacement as a generalized coordinate. In a load-displacement graph, the straight line from the origin to the point $(Q_{CR}, \delta_{CR})$ represents an upper-bound for all the possible equilibrium paths, as shown in Figure 1 (recent authors refer to as energy barriers [5], [6], [7]). A geometrically nonlinear analysis without imperfections would follow a lower stiffness path (blue dotted lines in Figure 1). This is due to the negative term of the geometric stiffness matrix, leading to the bifurcation point (marked by the blue triangle in Figure 1) associated with the global or local buckling branch. The bifurcated branches represent the only equilibrium space of the system, therefore the resulting equilibrium path must lay within those if the control parameters of the analysis are increased. A valley in the equilibrium path indicates the presence of a snap-through instability. In this scenario, the system reaches to the *next* stable position (undergoing significant displacements) on the positive slope portion of the valley at the same load level of the limit point. The presence of the imperfections (continuous blue line in Figure 1) further reduces the system stiffness, since they are usually introduced from a geometric

deviation proportional to a critical eigenshape (or a combination of them). $Q_{EBi}$ is therefore the limit point of the computed $i$ equilibrium path using $\Lambda_i$ as a load control analysis factor and a selected imperfections pattern. As illustrated in Figure 1b), $Q_{EB}$ may result higher than $Q_{CR}$ as a result of a hardening overall postbuckling branch. In such cases, the postbuckling behavior is classified as benign [8], since to an increase of the external load, the stable nature of the bifurcation branch does not change (as it occurs for the Euler beam). The structure collapse would then take place in the form of a material failure or in correspondence with a local buckling secondary branch (dark grey curves in Figure 1). The interaction between local and global instabilities is a largely studied topic and of the central importance of reticulated structures [9], [10], [11], [12], [13]. These local buckling branches have always a negative slope portion in the global generalized coordinates plane, due to effect of geometric nonlinearity, as evidenced by Gioncu [14], [15], [16]. Thompson theorems ([17], [18]), [19] allow the composition of the final equilibrium path starting from discrete branching analysis. Because the resultant from a positive and negative slope is a negative one, the overall bifurcated paths in Figure 1 are always unstable (dotted blue line). The effect of the imperfections can be measured through the erosion in the load curve between the limit point and the branch intersection cusps (more than one local buckling branch normally exists). Intuitively, sharper are these cusps deeper is the load erosion, meaning that the structure is more sensitive to geometrical imperfections. Moreover, to a vertical erosion corresponds an increase in the path curvature in proximity of the limit point, and therefore, a greater pre-buckling flexibility. Finally, a cusp bifurcation may occur as

the first equilibrium path bifurcation as in Figure 1a). In this case, the post-buckling is identified as catastrophic, or ultra-catastrophic when both the general coordinates reverse [8], [20]. In term of collapse mechanism, the limit point translates into the well known snap-through buckling phenomenon [21], [22], [23], [24]. Then, both the equilibrium paths in Figure 1 share such collapse mechanism, but with a profound difference in how it is triggered. A good indicator is the ratio $\frac{Q_{EB}}{Q_{CR}}$: when it is lower than 1, the corresponding equilibrium path exhibits both a higher imperfection sensitivity and a higher flexibility than the structures that have $\frac{Q_{EB}}{Q_{CR}} > 1$. In shell design, significant knockdown factors must be introduced to keep the structure at load levels safely below $Q_{CR}$ [25], [26]. Conversely, when $\frac{Q_{EB}}{Q_{CR}} > 1$, there is still room for postbuckling behaviour improvement through local buckling prevention strategies that retard the overall collapse [27], [28]. The occurrence of localized yielding increases the displacement response of the structure, therefore the elasto-plastic buckling load $Q_{EP}$, evaluated through a GMNIA, can be notably lower than $Q_{EBi}$. This is particularly relevant for flexible structures and with the presence of stress spikes. A good indicator for this vulnerability is the yielding load $Q_Y$: the level of external load at which the first yielding stress is reached in any of the gridshell elements (observered by Kato in [29]). Formal differences in the equilibrium path are given by three main factors, that drive the overall stability behaviour: geometry, imperfections and connections stiffness [30]. Concerning the former, comparisons between classical spatial configurations have evidenced that geometries with high membrane regime of internal forces (i.e. domes) exhibit smaller flexibility towards vertical loads but increased imperfection sensitivity [31]. At the same time,

they also display a formal behavior transition when the shallowness ratio is varied, contrary to bending driven geometries like barrel vaults. Such change resembles the fundamental observations for continuous shell buckling by Von Karman [32], and more recently summarized in [33], and for flat arch stability [34],[35]. Anyway, reticulated systems suffer local instability problems more than their continuous counterparts, such as connection failure or member (local) buckling, that can lead to progressive collapse of the whole compartment [36], [37], [13], [38]. Freefrom geometries have instead a less predictable behavior, because the force fluxes have not a straightforward path to the bearings [39]. Mesh pattern plays a significant role in directioning such fluxes, and stability of freeform gridshells can be altered by it within the same median surface [40]. Slenderness of the members is also a part of the geometrical arrangement of a gridshell, and its effect on the equilibrium path is both nonlinear and non monotonic when varied [41],[42]. However, section members have often architectural constraints in shape and size, and in general chosen towards a dead load minimization. This three level set of geometrical features (median surface, mesh, slenderness members) concur hierarchically in generating the tangential stiffness matrix along the equilibrium path [43], [44].

In this paper we tried to use qualitative studies of the equilibrium path shape as a powerful tool for the conceptual design of a gridshell, testing two different geometries generated through a Multiblody Rope Approach (MRA) [45] and its improved version (iMRA) [46]. The MRA is a form-finding methodology designed to define structural geometry [47] by dynamically solving a structural model consisting of falling masses connected by inextensible ropes

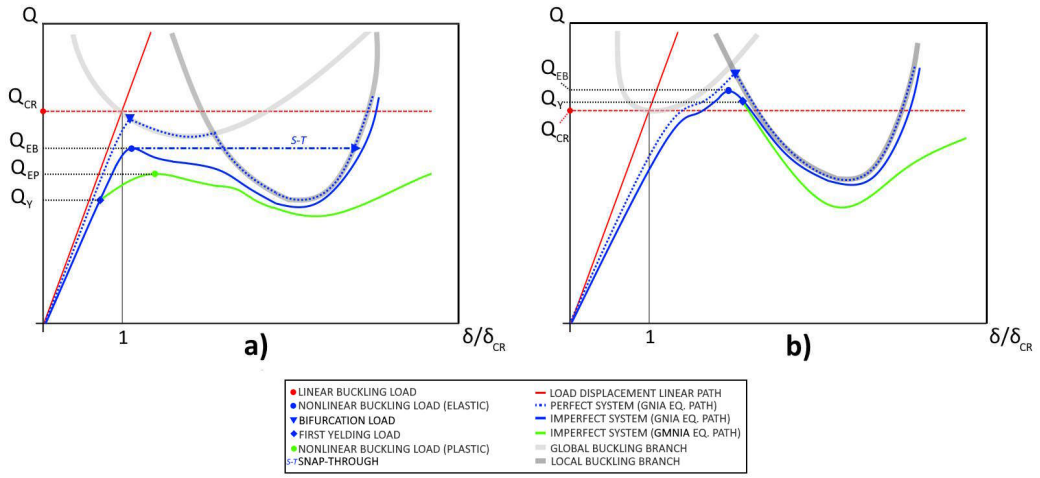


Figure 1: a) Equilibrium path of a reticulated shell with ultra-catastrophic post-buckling behavior. b) Benign (stiffening) postbuckling behavior.

[48, 49]. The i-MRA represents the enhanced version of the MRA [50]. The method is specifically designed for the form-finding and the optimization of the construction process of free-form gridshells [46]. A detailed study is conducted on the postbuckling behaviour of the geometries produced by these approaches [51]. In particular, we tested the influence of member slenderness through GNIAs and GMNIAs and several imperfection magnitudes for separate load patterns. We instead kept a unique initial tessellation and hypothesized a perfect rigid quadrangular connection.

## 2. Form-finding techniques

The Multibody Rope Approach (MRA) is a specialized method designed specifically for determining the funicular shape of free-form gridshells. In this form-finding method, the shape of the structure is derived by modelling a multi-body physical system. This system consists of nodal masses inter-

connected by slack ropes, each with a length equal to $l_{rope}$. The structural shape can be calculated by solving the dynamic model of the system 1 and applying D'Alembert's principle to determine the equilibrium of the system.

The solution can be obtained as:

$$\vec{u}(t) = C_1 e^{-2\omega_n \zeta} + C_2 + \frac{C_3}{2\omega_n \zeta} t \tag{1}$$

Where $C_1$, $C_2$ and $C_3$ are coefficients that can be calculated the system initial conditions.

$$C_1 = -\frac{2\omega_n \zeta \dot{\vec{u}}_{(t-\Delta t)} - C_3}{(2\omega_n \zeta)^2} \tag{2}$$

$$C_2 = -\frac{(2\omega_n \zeta)^2 \vec{u}_{(t-\Delta t)} + 2\omega_n \zeta \dot{\vec{u}}_{(t-\Delta t)} - C_3}{(2\omega_n \zeta)^2} \tag{3}$$

$$C_3 = \vec{p_i} + \sum_{j=1}^{n_i} \left\{ k \cdot \vec{F}_{rope,ji} \right\} \tag{4}$$

In Equation 1, $\vec{u}(t)$ represents the position of the nodal masses, where $t$ signifies the temporal instant at which the equation is computed. Additionally, $\omega_n = \sqrt{\frac{k}{m}}$ and $\zeta = \frac{c}{2\omega_n m}$ correspond to the natural frequency and critical damping of the system, respectively. These two quantities can be readily obtained by knowing the stiffness of the ropes $k$, the mass of the nodes $m$, and the damping coefficient of the system $c$.

In the equation 4, the vector $p_i$ represents the applied external force on a generic node $i$, while the forces transmitted by the ropes connected to the nodes are denoted by $\vec{F}rope, ji$. It is important to note that the reaction of

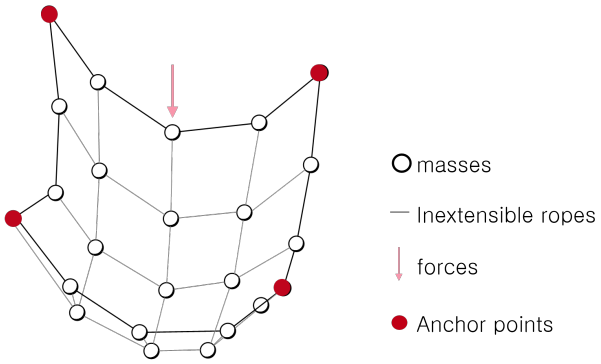


Figure 2: Dynamic model of falling bodies employed in the MRA and in the i-MRA.

the ropes can only be exerted when they are under tension. Thus, the forces $\vec{F}rope, ji$ can be derived as follows:

$$\begin{cases} F_{rope} = 0 & \text{if} \quad l < l_{rope} \\ F_{rope} = k(l - l_{rope}) & \text{if} \quad l \geq l_{rope} \end{cases} \tag{5}$$

Starting with a basic mesh, the final solution is calculated through a step-by-step process. The conditions at each step rely on the solution from the previous one.

In the final solution, structural components can be classified into two sets based on their length. Elements shorter than $l_{rope}$ are denoted as *loose elements* and those with a length matching $l_{rope}$ are labelled as *target elements*.

The i-MRA method stands as an advancement over the MRA, seeking not only to optimize geometry but also to improve the automation of the construction process by minimizing the variety of structural element typologies [46]. In particular, two key techniques are employed to achieve this optimization. The first involves grouping the structural elements and assign-

ing different slack coefficients to each group. In this case, starting from the solution derived by the MRA, a new equilibrium configuration is calculated using the subsequent formulation for the forces transmitted by the ropes, denoted as $\vec{F}_{rope,ji}$.

$$\begin{cases} F_{rope} = 0 & \text{if} \quad l < l_{rope,2} \\ F_{rope} = k(l - l_{rope,2}) & \text{if} \quad l_{rope,2} < l \leq \gamma(l_{rope,1} - l_{rope,2}) + l_{rope,2} \\ F_{rope} = 0 & \text{if} \quad \gamma(l_{rope,1} - l_{rope,2}) + l_{rope,2} < l < l_{rope,1} \\ F_{rope} = k(l - l_{rope,1}) & \text{if} \quad l \geq l_{rope,1} \end{cases} \tag{6}$$

In Equation 6, the terms $l_{\text{rope,1}}$, $l_{\text{rope,2}}$, ..., $l_{\text{rope,n}}$ represent the lengths of the ropes belonging to various groups.

Through an iterative process, a funicular configuration is determined where the majority of the ropes, representing the structural elements, are tensioned. then, the final model undergoes slight geometric variations through the application of a repulsive force field on the nodal masses. This causes the nodes to move away from each other and also tensions the remaining slack ropes. The application of this method involves incorporating into the external forces $p_i$ an additional contribution $q_i$, which represents the repulsive forces as defined in Equation 7.

$$q_i = -k_{rep}(l_{rope} - l_{ij}) \tag{7}$$

The combination of these techniques enables the grouping of structural elements by length and, consequently, minimizes the number of beam typologies required for the completion of the gridshell.

Figure 3: Islamic cultural center in Dakar, Senegal.

## 3. Case Study: The Dakar Mosque

The case study outlined in this paper focuses on the roof of the Islamic Cultural Center in Dakar, Senegal. The roof of the mosque, depicted in Figure 3, is designed by the architectural firm Fragomeli+Partners [52] in collaboration with Wafai Architecture. The distinctive roof design draws inspiration from the desert dunes, harmonizing with the surrounding environment.

### *3.1. Geometry Outline*

The design of the Dakar mosque roof consists of a steel gridshell spanning meters 63 meters by 56 meters. The shape is defined with the aim of creating a free span, resting solely along its perimeter, eliminating the need for intermediate pillars, as depicted in Figure 4.

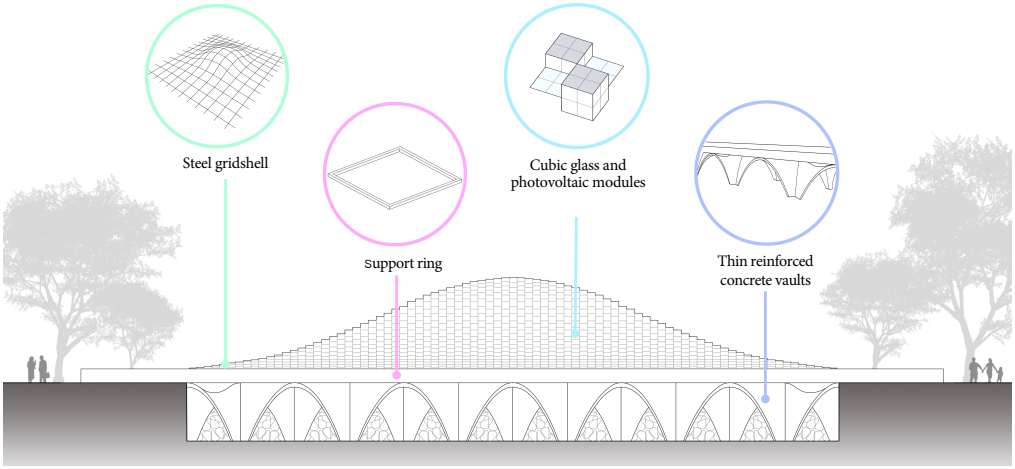


Figure 4: The concept behind the structural design of the Dakar Mosque.

Such geometry is primarily influenced by architectural design, introducing specific constraints, including a distinctive curvature that distinguishes it from conventional vaulted structures.

These constraints have significant implications for both the quantitative and qualitative aspects of structural behaviour characteristics. In general, the form-finding process involves applying the loads that act on the structure permanently to the numerical model. This allows for defining a structural form that is a funicular shape with respect to the loads that predominantly act on the structure during its service life. In the specific case of the roof of the Dakar mosque, to meet the architectural requirements, a load field different from the one actually experienced by the structure was required (as depicted in Figure 5). This deviation of the force field from the real one allows for achieving the curvature inversion regions that characterize the shape of the desert dune requested by the architects. At the same time, this change defines a structural form that is no longer funicular with respect to

the actual permanent loads. Therefore, the structural form with curvature change is less-than-optimal compared to the funicular form.

In this paper, two distinct form-finding methodologies were employed to establish the shape of the roof. The form-finding methodologies are used to define optimal geometries, notwithstanding the above mentioned constraints.

In particular, the application of the Multibody Rope Approach (MRA) [48] and the improved Multibody Rope Approach (i-MRA) [46] enables the derivation of a geometry that achieves a structurally feasible configuration while preserving the initial architectural design.

A parametric model of the structure was defined to derive the dynamic hanging net model subject to the load system depicted in Figure 5. By applying the MRA and i-MRA techniques to solve the equilibrium of the system, two configurations were obtained, both aligned with the vision of the architectural designer.

The Dakar mosque case presents a clear distinction in the geometries resulting from the utilization of the MRA and i-MRA form-finding methods. The MRA technique results in a configuration with a structural hierarchy where the main bearing structure is the central arch (Figure 6a). The structural elements required to construct the MRA shape are distinguished by 19

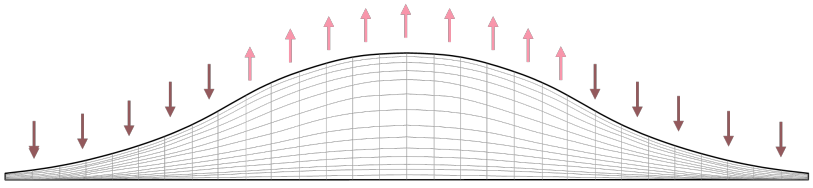

Figure 5: Force field applied to define architectural design.

different lengths.

In comparison, the i-MRA approach creates a smoother and regular geometry (Figure 6b). In this configuration, there are no self-evident structural hierarchies.

The i-MRA method, being designed to maximize the tensioned ropes in the hanging net model, promotes a greater degree of uniformity in the final geometry. Thus, a larger number of elements are engaged in supporting the applied loads. Consequently, only 8 element typologies define the i-MRA geometry.

The distribution of various types of structural elements for the two distinct structural configurations is illustrated in Figure 7 through histograms. Specifically, the MRA method involves establishing a target length, which, in this case, was set at 2.00m. Implementing this method results in obtaining 954 elements, constituting 53% of the total elements, with a length precisely matching the set target. Conversely, the remaining 47% of structural elements exhibit lengths different from the target. These elements are characterized by 18 distinct lengths, ranging from a minimum of 1.78m to a maximum of 2.02m.

In the case of using i-MRA, it is possible to identify various target lengths. This allows grouping structural elements into a smaller number of types. In the specific case of the examined gridshell, four different target lengths were set at 1.85m, 1.90m, 1.95m, and 2.00m. In this scenario, it can be observed that 99% of structural elements have a length precisely matching one of these targets. This enabled the grouping of structural elements, reducing the number of different types from 19 to just 8.

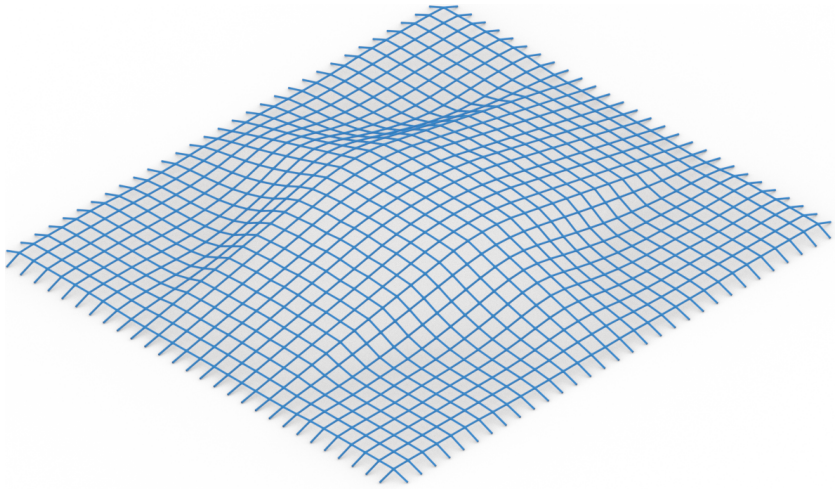

(a) MRA

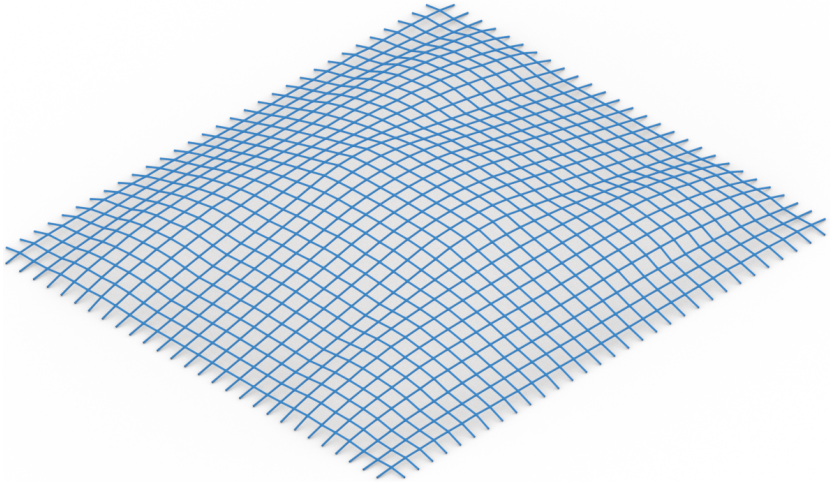

(b) i-MRA

Figure 6: Geometries obtained with the form-finding techniques.

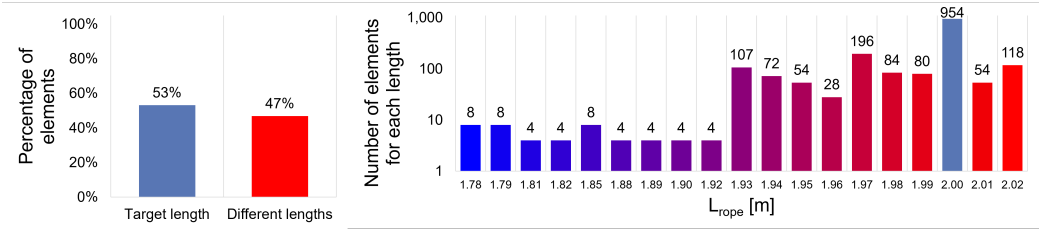


(a) MRA

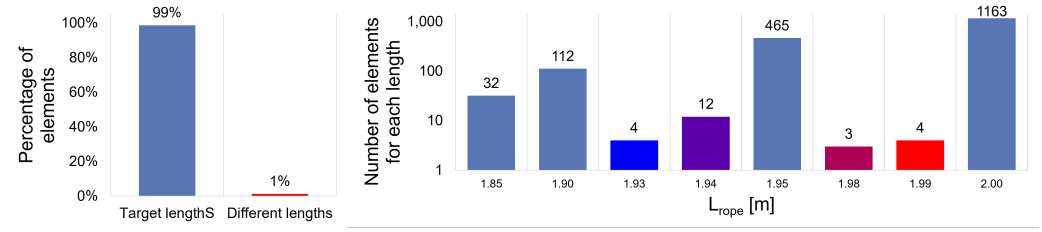


(b) i-MRA

Figure 7: Structural element typologies distribution in the two structural configurations.

### *3.2. Preliminary analyses*

We employed a finite element model of the gridshell by using quadratic three-node beam elements to investigate some fundamental structural properties. S355 steel circular hollow cross-section (CHS 19.1x8.0 mm) has been used and the base perimeter has been modelled as a series of full constraints.

The structural elements constituting both structures are fully constrained at their extremities. Choosing this type of constraint in a quadrangular mesh gridshell is essential for establishing a hyperstatic structural scheme. Indeed, opting for doubly hinged structural elements would result in a statically undetermined structural scheme.

In order to compare the two different shapes and evaluate the effects of geometric variations introduced by the i-MRA method, static and dynamic analyses have been conducted using the commercial finite element software

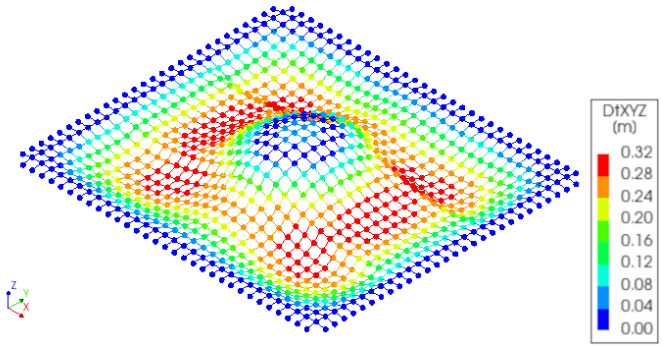


(a) MRA

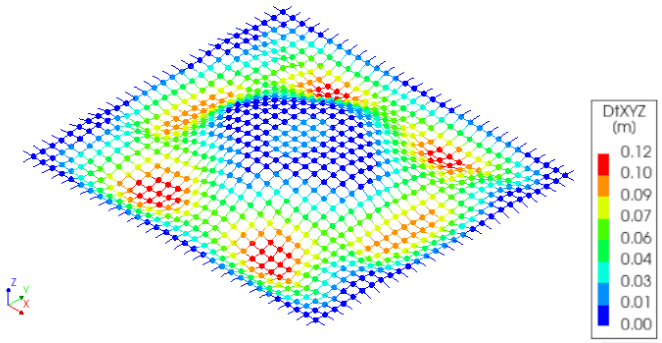


(b) i-MRA

Figure 8: Displacement due to self-weight.

Diana(R) (Dianafea bv, The Netherlands) [53]. Superstructure weight (solar glass panels) has been modelled as concentrated nodal loads, in addition to elements self-weight, considered as distributed.

In Figure 8 the displacement profiles obtained for the two geometries have been reported. for both cases, the maximum displacements occur at the curvature inversion regions of the roof. These areas represent structural weaknesses in terms of the response to vertical loading. Moreover, the

displacements are minimal near the supports and the central section of the structure, aligning with the expected behaviour. This emphasizes the rigidity of the central dome-like section compared to the curvature inversion zones. The behaviour validates the well-established effectiveness of vaulted structures in supporting vertical loads. Indeed, the larger displacements occur in areas where the roof deviates further from the dome-like geometry.

It is worth noting that the MRA shape exhibits a maximum displacement that is more than twice the value observed in the improved i-MRA case. However, even in the most extreme scenario, the maximum displacement remains well below 1/200th of the main roof span. Thus, the deformations observed in both cases are within acceptable limits and do not compromise the overall stability and functionality of the roof structure.

Figure 9 illustrates a comparative analysis of the reaction forces acting on the rigid supports.

A clear pattern emerges in the MRA-derived geometry. It is evident the presence of an arching behaviour along the main span direction, within a narrow central zone of the roof. Significantly lower reaction forces are observed on the supports not directly influenced by the central arch. This hierarchy in the reaction distribution implies that the central arch is mainly responsible for supporting the vertical loads.

In contrast, the support reactions are more equally distributed and balanced in the i-MRA shape.

Arching mechanisms are present in both horizontal directions, indicating bidirectional structural behaviour. The result is a more efficient load-sharing capacity of the second geometry.

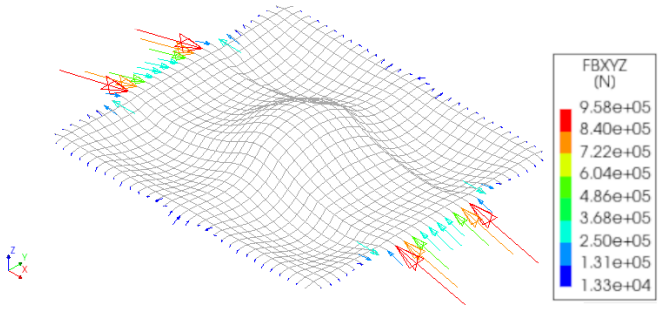


(a) MRA

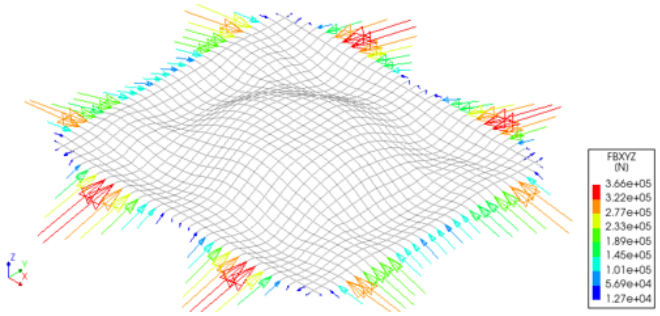


(b) i-MRA

Figure 9: Bearing reactions due to self-weight.

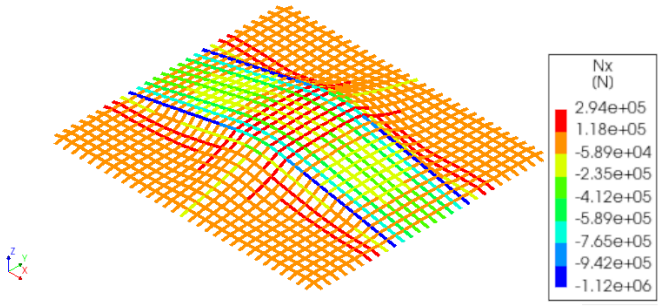


(a) MRA

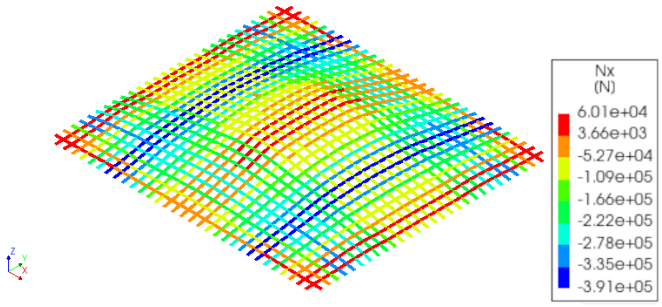


(b) i-MRA

Figure 10: Axial force in the structural elements due to self-weight.

The axial force and bending moment generated by dead loads are depicted in Figure 10 and 11, respectively. An obvious difference between the two designs emerges considering the internal force patterns.

In the MRA structure, higher compressive forces are concentrated in the central arch. In contrast, the lateral elements are either lightly loaded or subjected to tension.

The colour-scaled graph effectively visualizes these distinct structural hierarchies. Indeed, the compressed central arch appears clearly distinguished from the secondary elements.

By opposition, the i-MRA geometry demonstrates a more balanced load distribution. Compressed arches are present in both directions. This results in a significant reduction in the extent of tensile regions compared to the MRA case. Moreover, in the MRA geometry, the maximum compressive axial forces are three times higher than those observed in the i-MRA case. Similarly, the maximum tensile axial forces are almost five times greater.

Figure 11 shows that the structural elements experience bending moments in both the studied geometries.

As expected, the magnitude of bending moments within the gridshell is relatively small. Nevertheless, it is worth noting that the i-MRA configuration demonstrates improved performance in this regard. Specifically, the maximum bending moment observed in the MRA case is approximately twice the corresponding bending moment in the i-MRA geometry. This discrepancy indicates that the i-MRA approach achieves a more balanced distribution of bending moments, leading to a more efficient and optimized configuration.

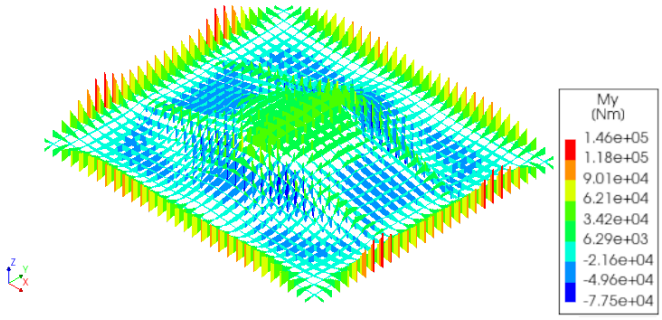


(a) MRA

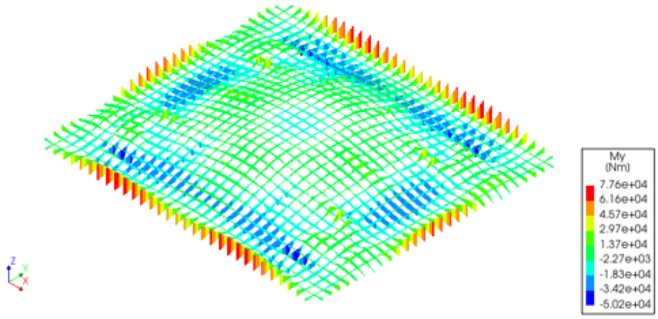


(b) i-MRA

Figure 11: Bending moment in the structural elements due to self-weight.

Considering the static analyses, it can be concluded that the i-MRA configuration leads to a more balanced distribution of forces. Thus, the i-MRA method demonstrates its ability to reduce structural hierarchies and enhance the overall performance of the structure.

Finally, the comparison between the two geometries in terms of modal frequencies and modal shapes is reported. The free vibration analysis of the gridshells shows that they have similar eigenvalues (frequencies), as reported in Table 1. However, the first eigenshapes reported in Figure 12 demonstrate two different configurations. In particular, the eigenshape associated with the MRA geometry exhibits higher deformation in the curvature inversion region. In contrast, the i-MRA configuration reveals four distinct structural zones where deformations are symmetrically distributed around the central axes.

Furthermore, the i-MRA shape demonstrates a generalized frequency shift of approximately -0.1 Hz compared to the MRA configuration. Thus, the geometric variations introduced by the i-MRA method induce a slight modification in the dynamic response, in favour of a higher overall stiffness.

| **Mode** | **MRA** | **i-MRA** | **Mode** | **MRA** | **i-MRA** |
|---|---|---|---|---|---|
| 1 | 1.03E+00 | 9.09E-01 | 11 | 2.11E+00 | 1.85E+00 |
| 2 | 1.07E+00 | 1.06E+00 | 12 | 2.21E+00 | 2.03E+00 |
| 3 | 1.08E+00 | 1.14E+00 | 13 | 2.25E+00 | 2.25E+00 |
| 4 | 1.18E+00 | 1.27E+00 | 14 | 2.52E+00 | 2.26E+00 |
| 5 | 1.81E+00 | 1.52E+00 | 15 | 2.75E+00 | 2.28E+00 |
| 6 | 1.83E+00 | 1.53E+00 | 16 | 2.82E+00 | 2.45E+00 |
| 7 | 1.88E+00 | 1.64E+00 | 17 | 2.89E+00 | 2.73E+00 |
| 8 | 1.92E+00 | 1.72E+00 | 18 | 2.96E+00 | 2.74E+00 |
| 9 | 2.05E+00 | 1.81E+00 | 19 | 3.04E+00 | 2.84E+00 |
| 10 | 2.11E+00 | 1.83E+00 | 20 | 3.06E+00 | 2.85E+00 |

Table 1: Eigen-frenquencies obtained by the dynamic modal analysis.

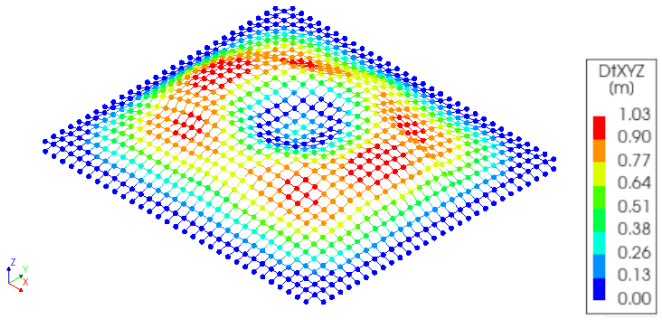


(a) MRA

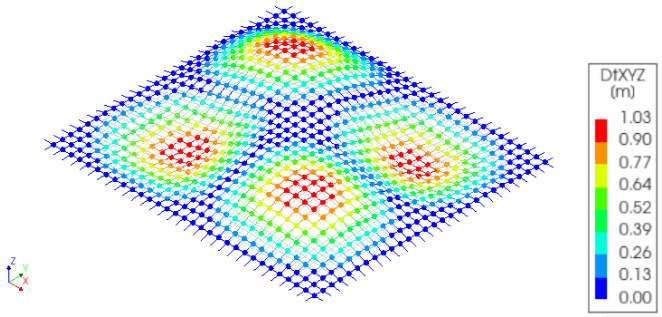


(b) i-MRA

Figure 12: Mode 1 eigen-shapes obtained with the dynamic modal analysis.

## 4. Equilibrium Paths

Moving ahead to a deeper structural analysis, the behaviour of the two configurations of the roof with respect to stability is now investigated. The finite element program LUSAS [54] has been used and the structures have been modelled by adopting finite elements with a formulation based on the modified Timoshenko hypothesis for thick beams to the continuum theory. In the adopted formulation, the deformation due to shear is considered and the cross-sections remain plane and undistorted under deformation but do not remain normal to the beam axis. In the model, each structural element is divided into 4 different finite elements adopting a 4 nodal mesh. Analogous static schemes and material characteristics to previously described analyses have been employed.

In order to study the effects of the elements slenderness on the instability phenomena, three different cross-sections were investigated. The slenderness ratio $\lambda = \sqrt{\frac{AL^2}{J}}$ is defined as a function of the cross-section area $A$, structural elements length $L$ and bending inertia $J$. In the case studies, a standardized length was employed for the definition of the slenderness ratio. This adopted length is the predominant dimension among the elements in both structures. Specifically, this length aligns with the target length used in the MRA, established at $L = 2.00m$. The dimensions of the tubular cross-section have been chosen to investigate three possible slenderness ratios with $\lambda$ values of 50, 100, and 150.

Three different magnitudes of imperfection have been evaluated. The purpose is to assess the effects of geometric variations introduced during the construction phase on the instability phenomena.

In particular, the geometry is deviated from the initial one considering the shape of the first buckling mode of the structure. The buckled geometry is scaled to investigate three possible maximum deviations. Operating this way, the obtained results provide an index about the imperfection sensitivity of the initial geometry, being the eigenshapes intrinsically connected to the geometric stiffness matrix $K_G$. The first scenario represents the maximum accepted tolerance during the construction phase, equal to 1 cm. In the remaining scenarios, the maximum deviations have been defined as a function of the structure free span. The reason is to consider potential flaws due to the complexity of realizing such an advanced structure. The, the maximum deviations are set equal to $L/1000 = 6cm$ and $L/500 = 12.5cm$.

Finally, two load patterns are investigated. In the first loading condition, vertical loads are uniformly distributed as concentrated forces acting on all the structural nodes. This configuration represents the most common loading condition during the structure service life. Actually, the structure is always subject to self-weight and permanent.

The second scenario focuses on a situation where just half of the structure is subjected to vertical loads. This condition is relevant as it represents an asymmetrical load scenario that can significantly impact the structural stability through force flows imbalance.

### *4.1. Linear Buckling*

In this section, the results of the linear eigenvalue buckling analysis of the two structural geometries under two different loading conditions are reported. The finite element models have been realized as described in Section 4 by using the software LUSAS [54]. Buckling state is reached through the

extraction of the eigenvalue $\lambda$ from the problem $det(K - \lambda K_G) = 0$, where $K$ and $K_G$ are the global and geometric stiffness matrices respectively. Lanczos solution method has been used and the error norm resulted in lower than $1E - 11$ for all the computed modes.

The first buckling mode of the two geometries is illustrated in Figure 13 and 14, respectively for the symmetrically and the asymmetrically distributed loads. The eigenshapes illustrated are the linear buckling deformations with the lowest energy. Consequently, they are utilized as a reference in investigating the impact of the imperfections on structural behaviour.

Finally, Table 2 presents the linear buckling eigenvalues for both structural configurations, considering three different slenderness ratios. The eigenvalues represent the critical load multipliers that lead to structural instability. As a result, the table reports the relative difference in load multiplier between the studied geometries.

The differences, denoted as $\Delta$, are computed as percentages. This calculation is performed according to Equation 8, where $\omega_{MRA}$ represents the buckling load multipliers associated with the MRA structure, and $\omega_{i-MRA}$ corresponds to those related to the i-MRA structure.

$$\Delta[\%] = 100 \left( 1 - \frac{\omega_{MRA}}{\omega_{i-MRA}} \right) \tag{8}$$

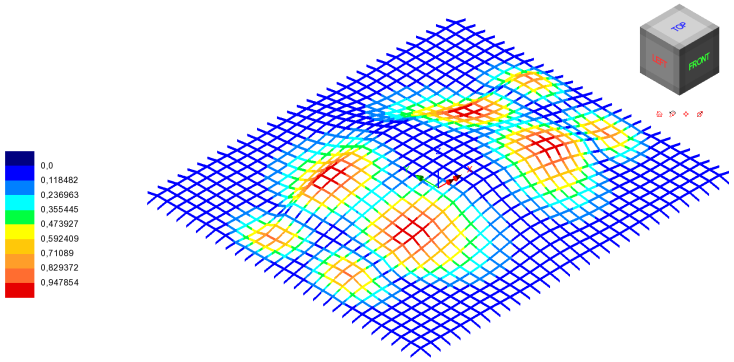


(a) MRA

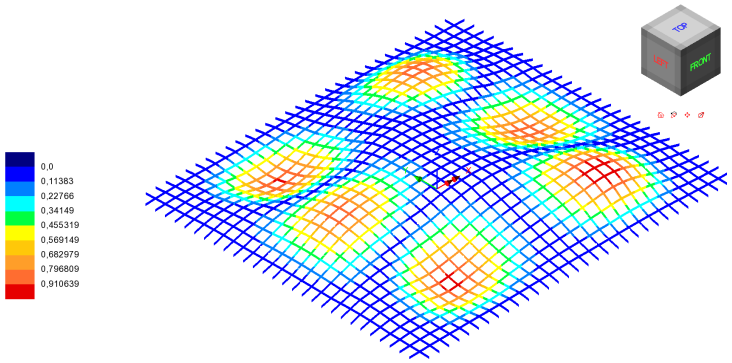


(b) i-MRAd

Figure 13: Mode 1 eigen-shapes obtained with linear buckling analysis on the symmetrical loaded structures.

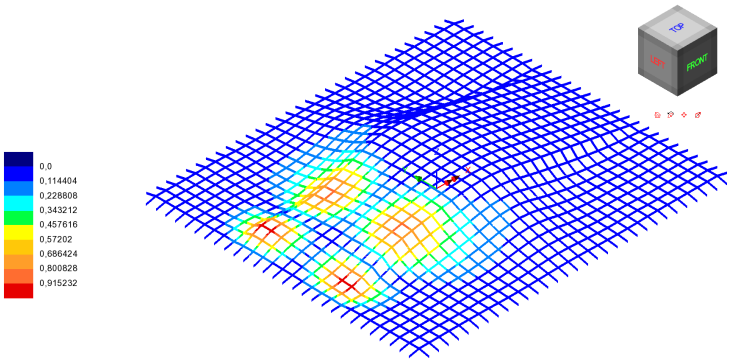


(a) MRA

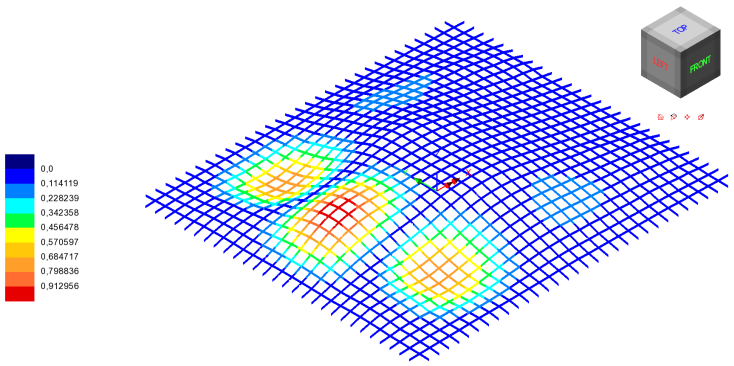


(b) i-MRA

Figure 14: Mode 1 eigen-shapes obtained with linear buckling analysis on the asymmetrical loaded structures.

| | | MRA | | i-MRA | | Difference % | |
|---|---|---|---|---|---|---|---|
| $\lambda$ | **Mode** | **Sym** | **Asym** | **Sym** | **Asym** | **Sym** | **Asym** |
| **50** | **1** | 1935.7 | 3041.6 | 1204.1 | 1412.8 | 37.8% | 53.6% |
| | **2** | 1973.3 | 3454.8 | 1305.2 | 1502.8 | 33.9% | 56.5% |
| | **3** | 2194.0 | 3795.0 | 1351.1 | 1664.2 | 38.4% | 56.1% |
| **100** | **1** | 94.8 | 156.0 | 72.7 | 91.1 | 23.3% | 41.6% |
| | **2** | 97.8 | 174.3 | 77.3 | 94.4 | 21.0% | 45.8% |
| | **3** | 104.5 | 192.4 | 78.3 | 100.2 | 25.1% | 47.9% |
| **150** | **1** | 17.4 | 27.6 | 14.0 | 18.6 | 19.5% | 32.6% |
| | **2** | 18 | 30.6 | 14.2 | 18.9 | 21.1% | 38.2% |
| | **3** | 18.9 | 33.1 | 14.4 | 19.8 | 23.8% | 40.2% |

Table 2: Dakar Mosque linear buckling eigenvalues (load multipliers) considering symmetric and asymmetric load condition.

### *4.2. GNIAs*

To investigate the post-buckling behaviour of the structure, an incremental load Geometrically Nonlinear Analysis with Imperfections (GNIA) has been conducted. The co-rotational formulation [55] has been employed to account for geometrical non-linearity. Body strains have been derived at each step from the rigid body motion, considering both the element and the force vector rotation. Step by step, therefore the geometric stiffness matrix has been computed taking into account the elements rotations and deformations, and consequently the equilibrium paths have been outlined.

Imperfections have been modeled using the first linear buckling mode associated with each loading condition. The eigenshapes have been scaled to have a maximum deviation from the original geometry as defined in 4.

The GNIA has been performed to determine the loading path considering both the symmetrical and the asymmetrical loading patterns. The analyses have been then repeated in order to asses the effects of geometrical imperfections and changes in the structural element slenderness.

The initial study was conducted by varying the slenderness of the structural components while maintaining constant the imperfection. The displacement-load paths of the gridshells with a maximum geometric imperfection of 1 cm are presented in Figure 15. In the graphs, the sum of the structural element reactions $F_z$ to the applied loads $Q$ is shown as a function of the displacement of the central structural node $\delta$. Results are reported for both geometries, considering two distinct loading conditions and three different element slenderness $\lambda$. Furthermore, to emphasize the relationship between the linear buckling and the nonlinear load path, the linear buckling load is depicted as

a dashed horizontal line.

In Table 3, the results of the analyses are reported in terms of Euler load $Q_{CR}$, elastic buckling load $Q_{EB}$ and Yielding load $Q_y$. These loads represent critical situations in terms of structural integrity. For this reason in the Table is also reported the design load $Q_d$ defined as $min\{Q_{CR}, Q_{EB}, Q_y\}$.

In the table, a comparison is made between the two structures, considering the relative difference for each critical loading situation. Specifically, the differences, denoted as $\Delta_Q$, are reported as percentages and calculated as per Equation 9, where $Q$ represents $Q_{CR}$, $Q_{EB}$, $Q_y$, or $Q_d$, depending on the specific situation under consideration.

$$\Delta_Q[\%] = 100 \left(1 - \frac{Q_{MRA}}{Q_{i-MRA}}\right) \tag{9}$$

It is worth noting that the numbers in the table represent vertical loads that are deemed positive when acting in the direction of gravity acceleration.

It should be highlighted that the yielding load $Q_y$ is the lower critical load for the MRA case, considering all the possible slenderness values. Thus, the stress distribution considering the minimum between the Euler load $Q_{CR}$ and the elastic buckling load $Q_{EB}$ is computed. The stress distribution related to the structures with a slenderness $\lambda = 100$ is reported in Figures 16 and 17.

Moreover, the displacements to this loading condition with a slenderness $\lambda = 100$ is reported in Figures 18 and 19. The displacement configuration is key to understand the structural behaviour in the critical loading conditions.

Finally, the displacement-load paths have been extracted for increasing magnitude of imperfections. The first linear buckling eigen-shape has been

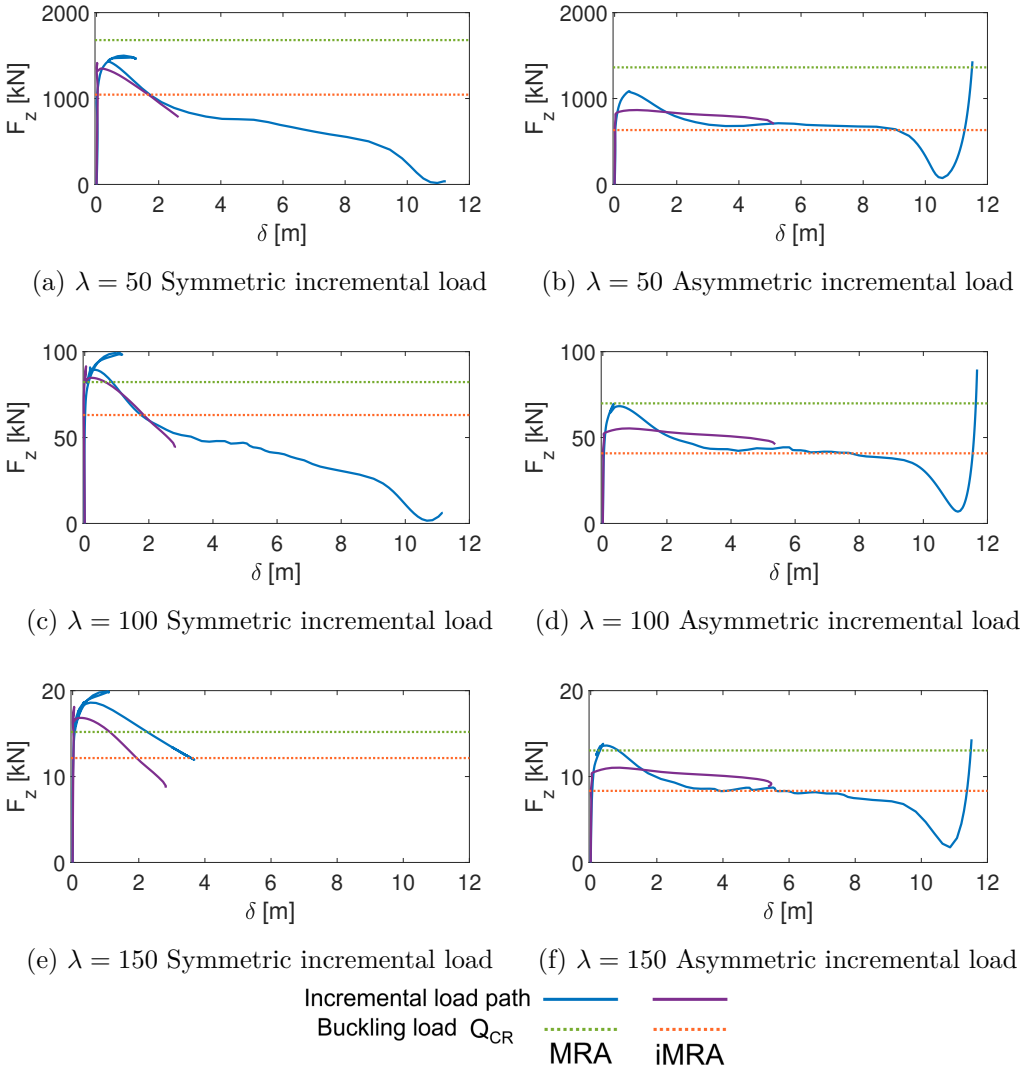


(a) $\lambda = 50$ Symmetric incremental load

(b) $\lambda = 50$ Asymmetric incremental load

(c) $\lambda = 100$ Symmetric incremental load

(d) $\lambda = 100$ Asymmetric incremental load

(e) $\lambda = 150$ Symmetric incremental load

(f) $\lambda = 150$ Asymmetric incremental load

Figure 15: Displacement-load path of the central node of the Dakar mosque gridshell considering an incremental load geometric nonlinear analysis.

| | $\lambda$ | **MRA** | | **iMRA** | | **Difference [%]** | |
|---|---|---|---|---|---|---|---|
| | | **Sym** | **Asym** | **Symmc** | **Asym** | **Sym** | **Asym** |
| $Q_{CR}$ | | 1680.1 | 1362.6 | 1045.2 | 632.9 | 37.8% | 53.6% |
| $Q_{EB}$ | **50** | 1428.2 | 1084.3 | 1349.0 | 866.0 | 5.5% | 20.1% |
| $Q_y$ | | **607.6** | **343.2** | **925.3** | **483.8** | -52.3% | -41.0% |
| $Q_{CR}$ | | 82.3 | 69.9 | **63.1** | **40.8** | 23.3% | 41.6% |
| $Q_{EB}$ | **100** | 90.9 | 68.2 | 84.8 | 55.3 | 6.7% | 18.9% |
| $Q_y$ | | **75.0** | **43.2** | 83.2 | 51.3 | -11.0% | -18.7% |
| $Q_{CR}$ | | **15.2** | 13.0 | **12.2** | **8.3** | 20.0% | 36.1% |
| $Q_{EB}$ | **150** | 18.6 | 13.6 | 16.8 | 11.0 | 9.3% | 19.1% |
| $Q_y$ | | **15.2** | **10.8** | 16.5 | 10.1 | -8.5% | 6.6% |
| | **50** | 607.6 | 343.2 | 925.3 | 483.8 | -52.3% | -41.0% |
| $Q_d$ | **100** | 75.0 | 43.2 | 63.1 | 40.8 | 15.9% | 5.6% |
| | **150** | 15.2 | 10.7968 | 12.2 | 8.3 | 20.1% | 22.8% |

Table 3: Critical instability loads in [N] considering the structural element slenderness $\lambda = [50, 100, 150]$ and both symmetrical and asymmetrical load patterns.

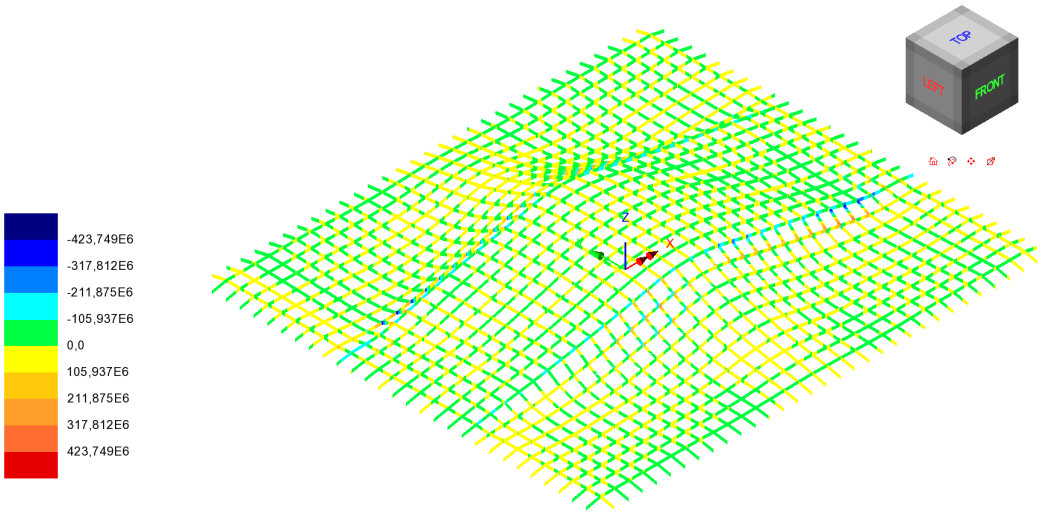


(a) MRA: $|\sigma_z| = 424MPa$

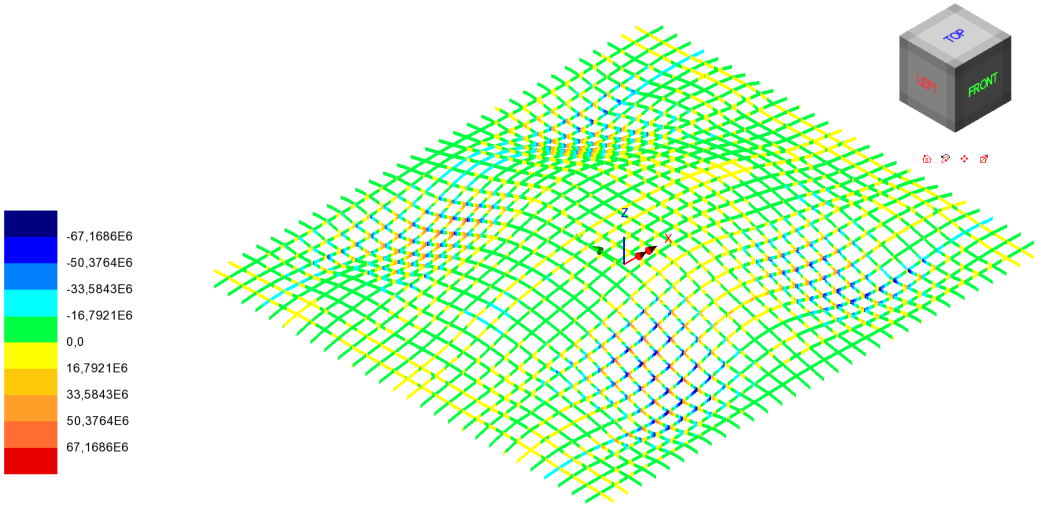


(b) i-MRA: $|\sigma_z| = 67MPa$

Figure 16: Stress distribution [MPa] related to the minimum critical load between Euler load $Q_{CR}$ and the elastic buckling load $Q_{EB}$ in the symmetrical load configuration.

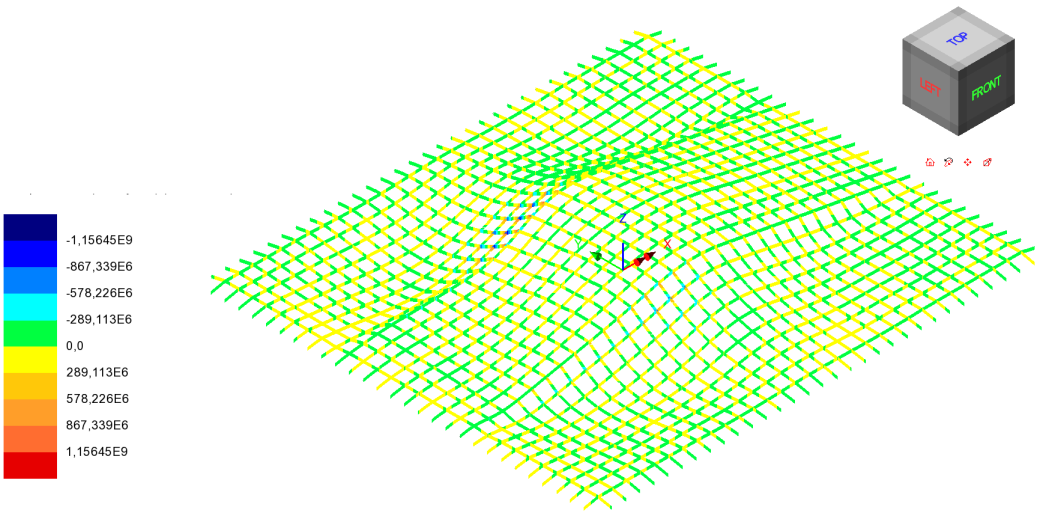


(a) MRA: $|\sigma_z| = 1157MPa$

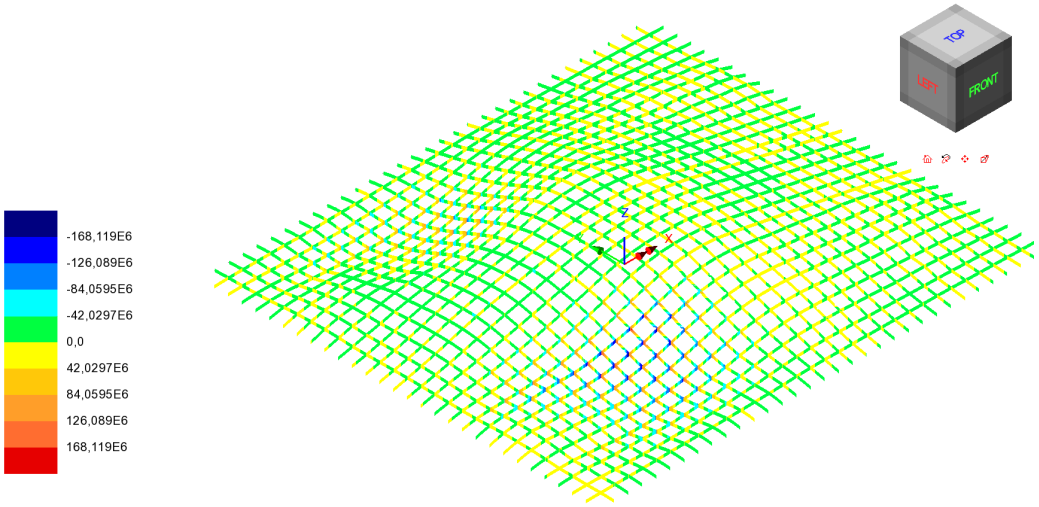


(b) i-MRA: $|\sigma_z| = 168MPa$

Figure 17: Stress distribution [MPa] related to the minimum critical load between Euler load $Q_{CR}$ and the elastic buckling load $Q_{EB}$ in the asymmetrical load configuration.

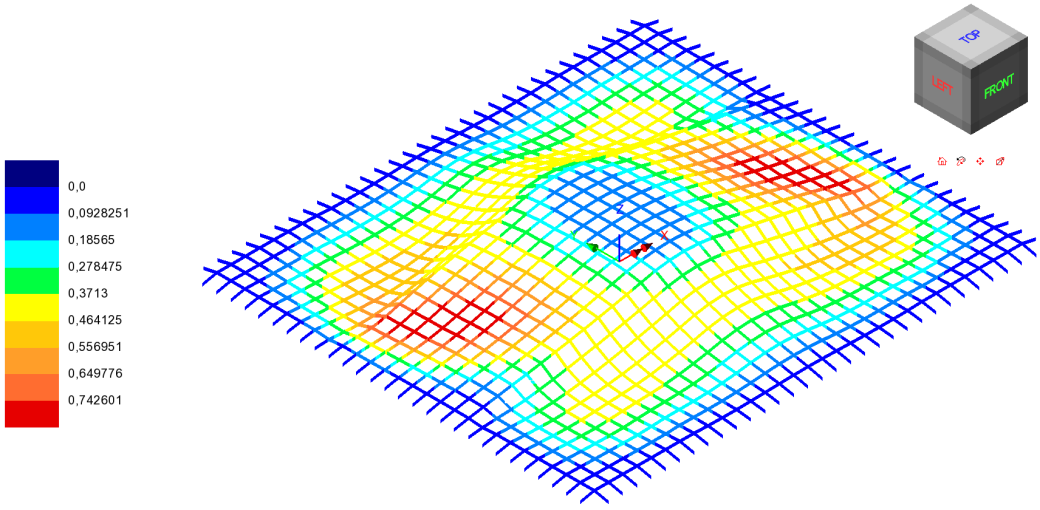


(a) MRA

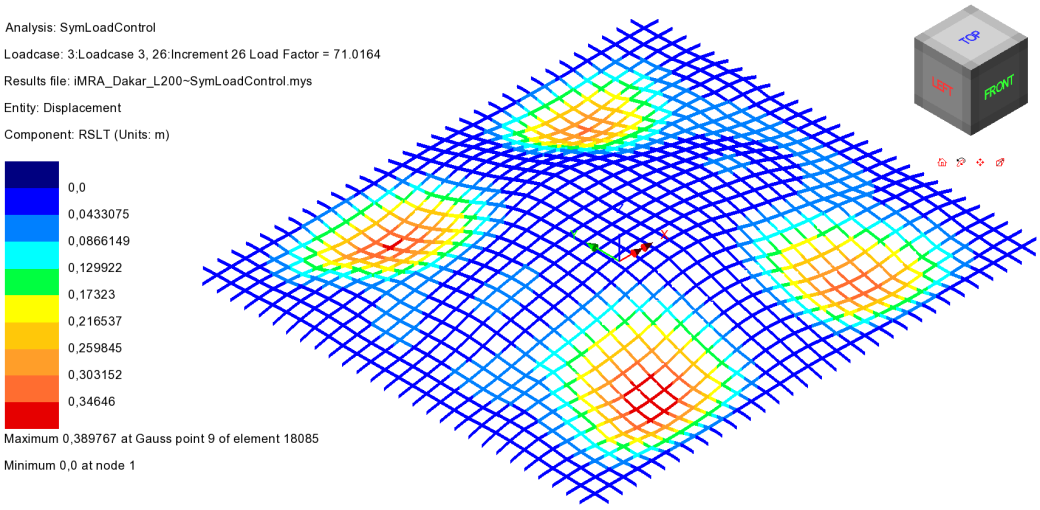


(b) i-MRA

Figure 18: Displacement distribution [m] related to the minimum critical load between Euler load $Q_{CR}$ and the elastic buckling load $Q_{EB}$ in the symmetrical load configuration.

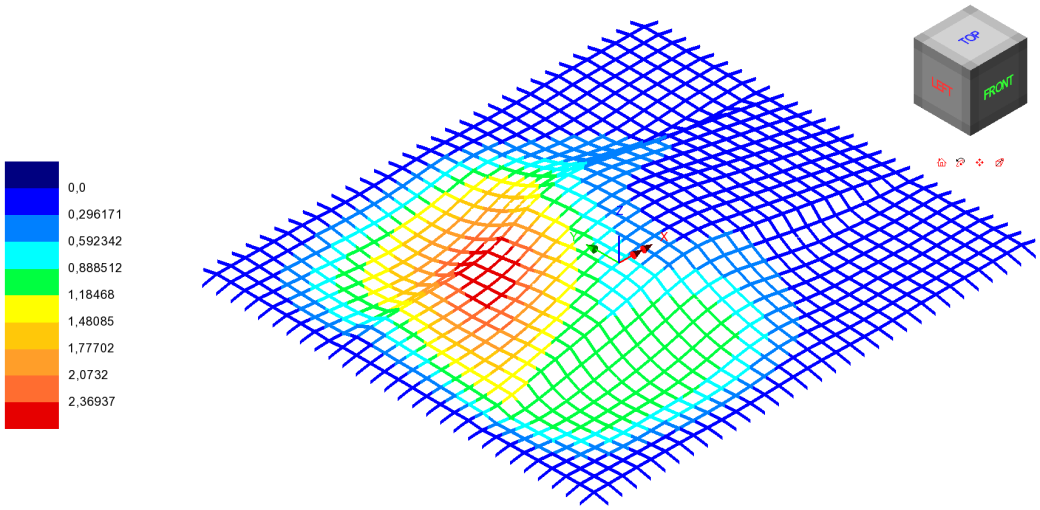


(a) MRA

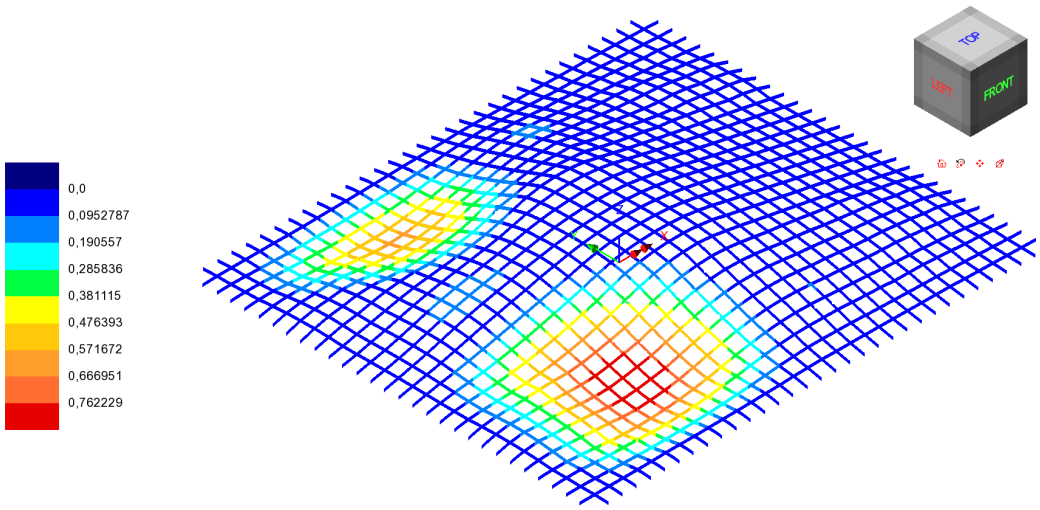


(b) i-MRA

Figure 19: Displacement distribution [m] related to the minimum critical load between Euler load $Q_{CR}$ and the elastic buckling load $Q_{EB}$ in the asymmetrical load configuration.

used to define the geometrical imperfections. The results for maximum deviations of $1cm$, $L/1000 = 6cm$ and $L/500 = 12.5cm$ are shown in Figure 20. In this case, the slenderness of the structural elements has been kept constant and equal to $\lambda = 100$.

It should be highlighted that the monotonously increasing branch shown in Figure 20(a) represents an unstable equilibrium path. It is essential to note that this equilibrium path can only be realized in a numerical solution. In practice, the behaviour of the structure will always adhere to the stable equilibrium path. Consequently, during numerical simulations, after attempting to follow the unstable path, the system will return to find equilibrium configurations associated with the stable path.

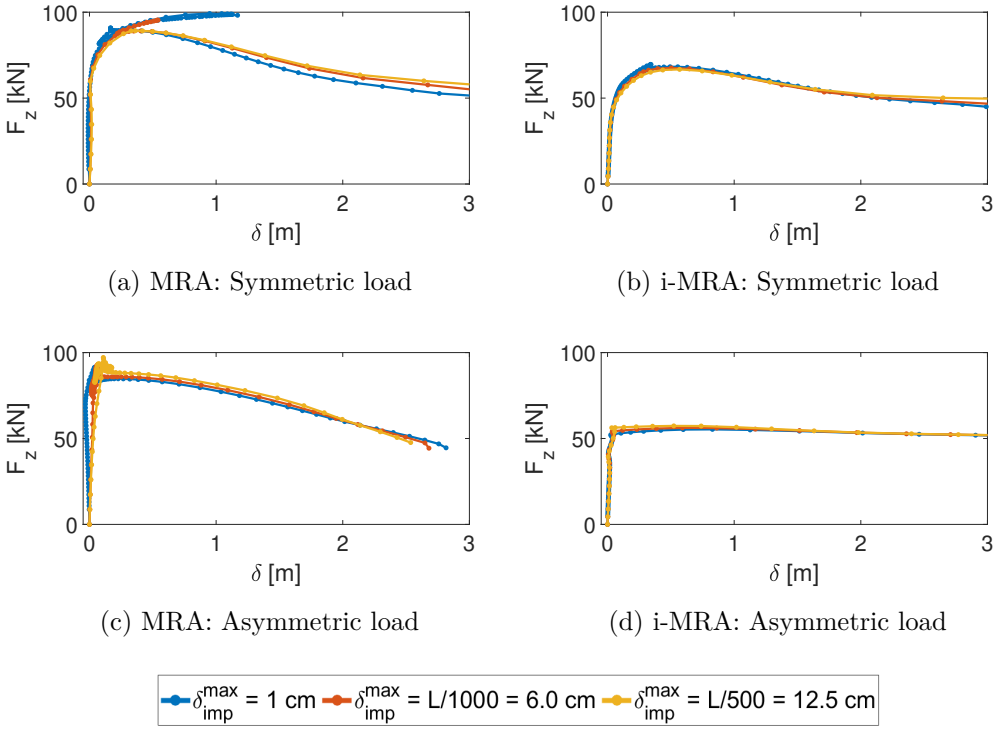


(a) MRA: Symmetric load

(b) i-MRA: Symmetric load

(c) MRA: Asymmetric load

(d) i-MRA: Asymmetric load

Figure 20: GNIA considering three magnitudes of imperfections on the Dakar mosque roof with $\lambda = 100$.

### *4.3. GMNIAs*

In Section 4.2, the GNIA findings demonstrates that the yielding load $Q_y$ and instability loads ($Q_{CR}$ and $Q_{ED}$) have the same order of magnitude. The structural elements in some regions of the structure may reach the yielding limit before the development of the instability phenomenon.

It is not possible to neglect the material non-linearity while investigating the interaction between yielding and instability. Indeed, the yielding of some structural components may alter the displacement field that is considered during the GNIA.

The elasto-plastic steel S355 constitutive law is added into the FEM to evaluate the effect of material non-linearity. An incremental load geometrically and material nonlinear with imperfection analysis (GMNIA) is performed on the structures with $\lambda = 100$. Initially, the structures with a maximum deflection equal to $1cm$ are investigated. The analysis is repeated for both the geometries and load configurations. In Figure 21, the GMNIA results are compared to those obtained with the GNIA. A dashed red line represents the $F_z$ value at which the yielding limit is exceeded. It is therefore possible to investigate how the structural behavior varies after passing yielding limit.

Finally, the analysis has been repeated for different magnitudes of imperfection to study the effects due to the combination of material non-linearity and geometric deviations. The resulting load paths are reported in Figure 22.

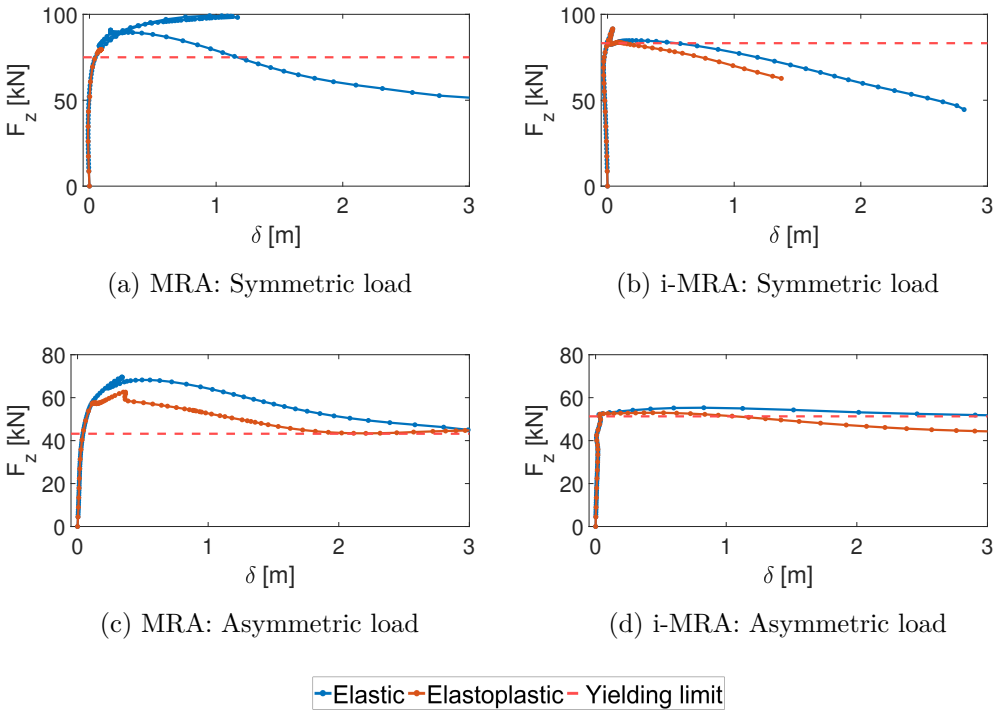


(a) MRA: Symmetric load

(b) i-MRA: Symmetric load

(c) MRA: Asymmetric load

(d) i-MRA: Asymmetric load

Figure 21: Comparison between GMNIAs with elastic and elasto-plastic material, $\lambda = 100$.

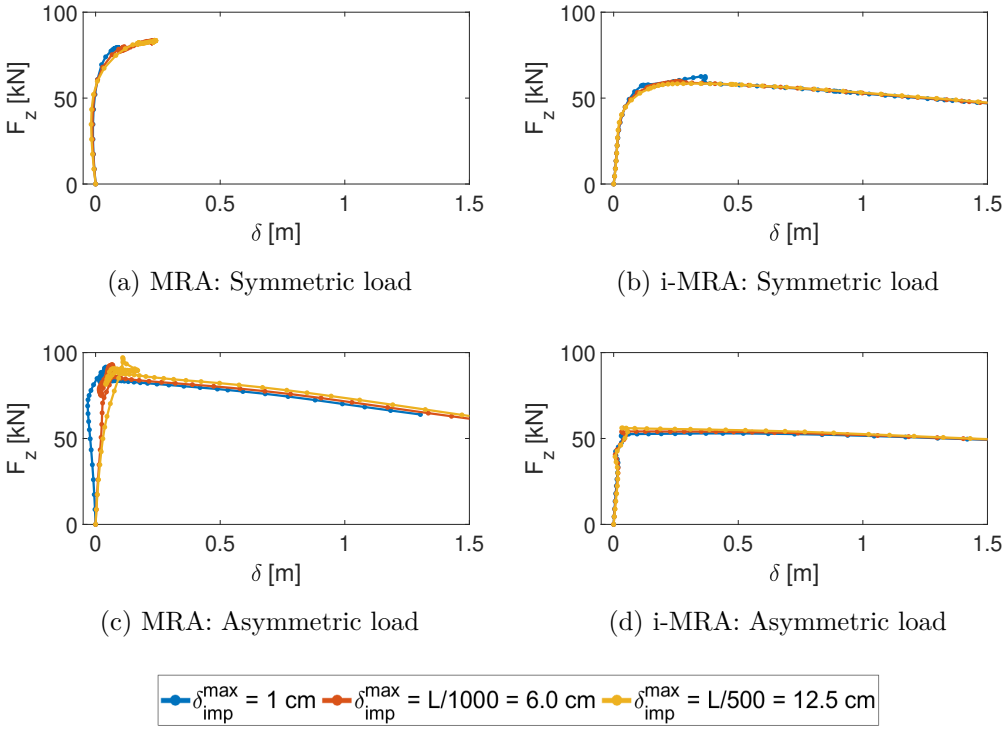


(a) MRA: Symmetric load

(b) i-MRA: Symmetric load

(c) MRA: Asymmetric load

(d) i-MRA: Asymmetric load

Figure 22: GMNIA considering elasto-plastic material and three magnitudes of imperfections on the Dakar mosque roof with $\lambda = 100$.

## 5. Discussion

The previous sections illustrate the results of the analyses carried out on the roof of the Dakar mosque. These studies investigated the influence of geometry, structural elements slenderness, material non-linearity, and imperfections on structural behaviour. The findings gathered from the analyzed data are detailed in the following.

### *5.1. Effect of geometry: MRA vs. iMRA*

The geometries generated using the two form-finding methodologies differ significantly in terms of response with respect to the instability phenomena.

The linear buckling analysis produces eigenshapes that have distinct deformations patterns. As a result, the linear instability behaviour in the two geometries is qualitatively different, as seen in Figure **??** and 14. The MRA case shows typical linear buckling of lowered arches, with the main deformations around the haunches of the central arch. This holds for both the studied load patterns. Instead, the buckling deformation in the i-MRA shape engages a greater number of structural members. Its behavior is similar to that seen in flat shell stability, or form resistance structures in general.

The eigenvalues provided in Table 2 reveal that the MRA structure performs better overall in terms of linear buckling resistance. Indeed, the critical loads $Q_{CR}$ are greater than those displayed by the i-MRA geometry for all the investigated scenarios. As introduced, this result can be invalidated by nonlinear analyses; when this happens, it generally implies for such cases the presence of catastrophic postbuckling behavior. However, the results of linear buckling analyses are essential to carry out the GNIAs. In details, they

have been used to define imperfection patterns, load patterns and factors.

In Section 4.2, the results of the GNIA for both the geometric configurations have been reported. The analyses allows for a meaningful comparison in terms of post-buckling behaviour. In the symmetrical load situation, the behaviour of the two geometries is remarkably similar, as evident in Figure 15. Even for the critical load $Q_CR$ is considerably different, the symmetrical equilibrium load path are similar. The differences in terms of elastic buckling load $Q_{EB}$ are smaller than 10%, as reported in Table 3. The postbuckling behaviour induced by the symmetric load pattern can classified as benign, since $Q_{EB} > Q_{CR}$ with the exception of the MRA case with $\lambda = 150$. This means that the equilibrium paths can be assimilated to those represented in Figure 1b).

It is worth noting that the differences in postbuckling behaviour become more pronounced when investigating the asymmetric loading case. In general, the critical loads are smaller when the load is distributed asymmetrically. Consequently, the asymmetrical loading condition results to be the critical one. The equilibrium paths in Figure 15 describe a very different exhibited behaviour by the two geometries. $Q_{EB} > Q_{CR}$ in the i-MRA structure indicates a benign postbuckling. In the MRA shape, however, $Q_{EB}$ is generally smaller than $Q_{CR}$. The structures exhibit catastrophic postbuckling behaviour. As a result, the equilibrium paths can be associated to the one represented in Figure 1a).

Figure 23 provides insights of the structure under asymmetrical loading conditions with $\lambda = 100$. The graph illustrates the evolution of displacements and stresses during the incremental load GNIA.

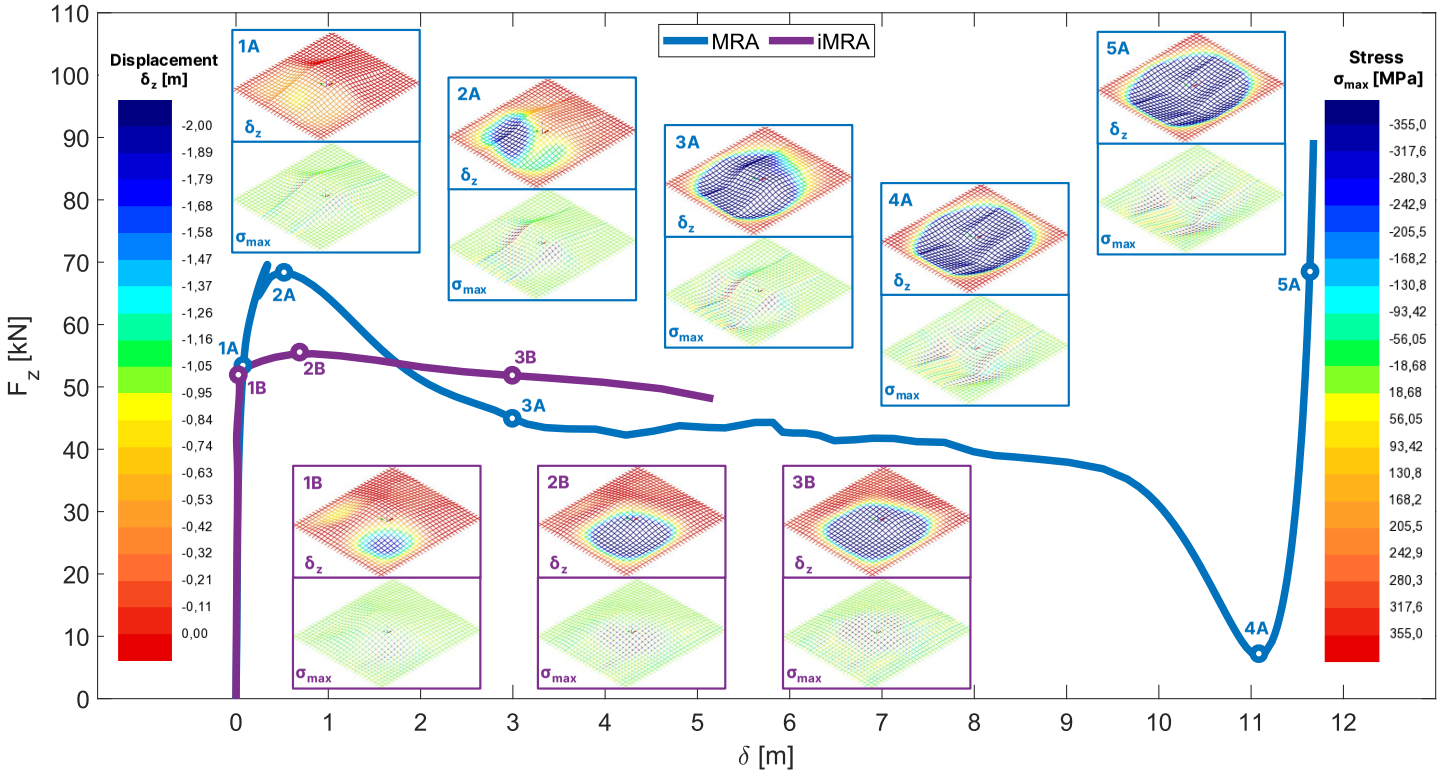


Figure 23: Postbuckling behaviour of the Dakar Mosque

In the initial phase, displacement increases approximately linearly as the load increases in both of the studied structures. Snap-through occurs in the MRA case with a sudden transition from peak configuration 2A to final configuration 5A. The collapse is catastrophic with a complete overturning of the roof.

Despite a reduced peak load $Q_{EB}$, the i-MRA configuration exhibits benign post-buckling performance. In the post-peak phase, the structure exhibits a plateau. The partial collapse experienced in the initial stages gradually extends. There is a smooth transition between a partial and global collapse.

The load-displacement graph in Figure 23 can be used to trace the collapse mechanism. The stress graphs illustrate that there is a larger concentration of stresses in the MRA case. As a result, the source of this concentration has been investigated, and the maximum axial force $N_{max}$ and bending moment $M_{max}$ have been computed for each load increment. Figures 24, 25, and 26 illustrate the values of $N_{max}$ and $M_{max}$ as the load increases. The Figures refer to structures with slenderness $\lambda$ 50, 100 and 150, respectively. In any case, it is clear that the maximum axial force and bending moment are always greater in the case of MRA than those on the i-MRA structure. This concentration implies that yielding will occur in specific structural nodes before the critical buckling load is attained.

In order to investigate the interaction between yielding and instability phenomena, the elasto-plastic constitutive law has been introduced in the model. In Figure 21 the elastic model is compared with the GMNIAs results.

Implementation of the elasto-plastic constitutive law to the MRA model

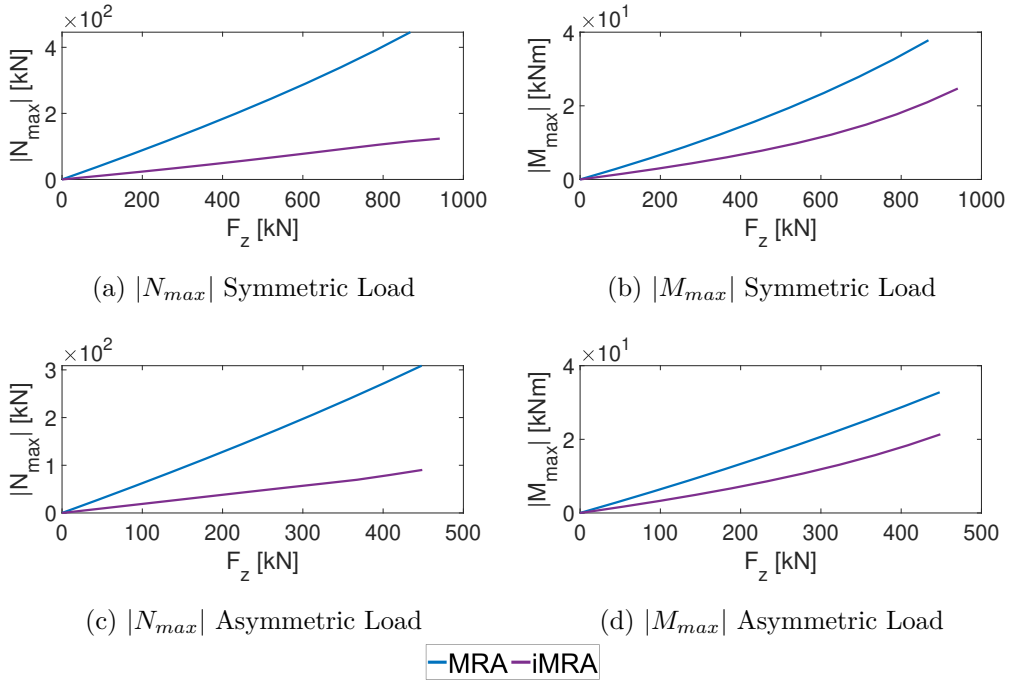


(a) $|N_{max}|$ Symmetric Load

(b) $|M_{max}|$ Symmetric Load

(c) $|N_{max}|$ Asymmetric Load

(d) $|M_{max}|$ Asymmetric Load

Figure 24: Maximum absolute axial force and bending moment in the structural elements with $\lambda = 50$ considering to increase the load to perform the GNIA.

reduces the linear buckling load, then results in $Q_{EB} < Q_{EP}$. In the case of i-MRA, yielding is observed in proximity to the elastic peak. As a result, the elastic buckling load $Q_{EB}$ is roughly equivalent to the elastic-plastic buckling load $Q_{EP}$. In either case, a reduction in stiffness is observed in the postbuckling tails.

### *5.2. Effect of member slenderness*

Structural members' slenderness effects have been investigated by analysing structures with three different $\lambda$. In particular, Table 2 reports the eigenvalues for the linear buckling analysis of structures characterised by $\lambda$ equal to 50, 100 and 150. The difference between the two structural configurations is

minimized when $\lambda$ increases, as seen in the Table. Local instability phenomena become more prevalent than global ones when slenderness rises. As a result, the effects of the geometric differences between the two configurations tend to be less significant.

Considering the GNIAs, In Figure 15 the same qualitative behaviour is observed for all the slenderness ratios. The major differences are related to the yielding load $Q_y$. In Table 3, the design load results to be the yielding one in the cases with thicker structural elements. For the i-MRA case, as the slenderness increases the instability becomes the most critical phenomenon.

At the same time, yielding seems to be the main challenge for all the slenderness ratios, if we consider the MRA geometry. This is a consequence of the stress concentration observed in Figures 16 and 17.

### *5.3. Effect of material yelding*

The GNIA results show that the yielding load $Q_y$ is the most critical in some of the investigated structural configurations. In particular, in the MRA case, it is observed that the $Q_y < Q_{EB}$ for all the slenderness ratios. In order to understand the effects related to material non-linearity, the elasto-plastic constitutive law has been included in GMNIAs. The results of the GMNIAs are shown in Figure 21, demonstrating that the yielding of the structural nodes can alter the structural behaviour.

In the MRA case is evident that after the yielding the global structural stiffness decreases. As a result, it is observed that $Q_{EP} < Q_{EB}$.

Considering the MRA geometry, the material non-linearity effects are exploited only on the postbuckling load paths. The stiffness decreases only after the peak and $Q_{EP} \approx Q_{EB}$.

The yielding of some structural nodes reduces the peak load in comparison to the MRA situation. In contrast, there is no significant effect on the behaviour of the i-MRA structure. Although in GNIAs the peak load of the MRA case was much higher, the concentration of stresses produced by such geometry results in the yielding of structural nodes prior to the establishment of buckling mechanisms. As a result of introducing an elasto-plastic constitutive law, the disparity between the two peak loads relative to the two analyzed geometries is greatly reduced due to local plastic flows.

### *5.4. Imperfection Sensitivity*

The structure defined by $\lambda = 100$ was examined by taking into account different levels of deviation from the basic geometry. The geometric imperfections were introduced by scaling the deformed relative to the first linear buckling mode. The resulting geometry was scaled so that the maximum distance between the deformed and undeformed configurations was 1 cm, $L/1000 = 6.0cm$, and $L/500 = 12.5cm$.

A geometrically nonlinear analysis with imperfection was conducted on the deformed configurations. The results of this analysis are shown in Figure 20.

The graphs indicate the presence of geometric deviations causes minor changes to the equilibrium paths. Deviations from the initial geometry appear to increase the peak load. This phenomena has been widely documented in the literature [56].

Finally, the analyses have been repeated after introducing material nonlinearity of the material; results are reported in Figure 22. Also in this case a slight improvement in the peak load is observed as the geometric deviation

620 increases.

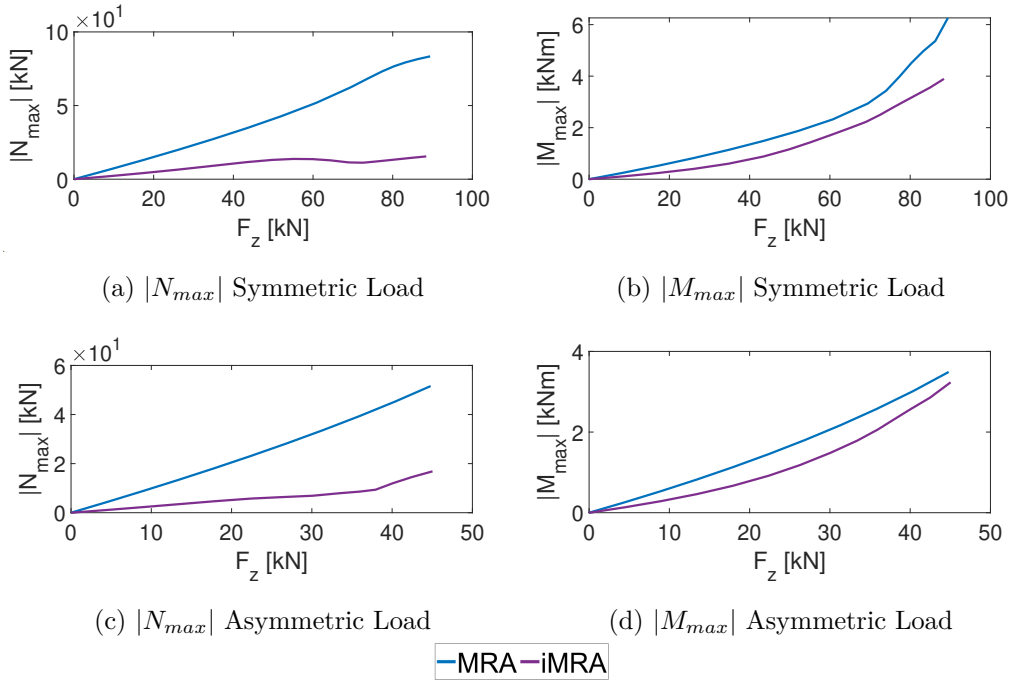


(a) $|N_{max}|$ Symmetric Load

(b) $|M_{max}|$ Symmetric Load

(c) $|N_{max}|$ Asymmetric Load

(d) $|M_{max}|$ Asymmetric Load

Figure 25: Maximum absolute axial force and bending moment in the structural elements with $\lambda = 100$ considering to increase the load to perform the GNIA.

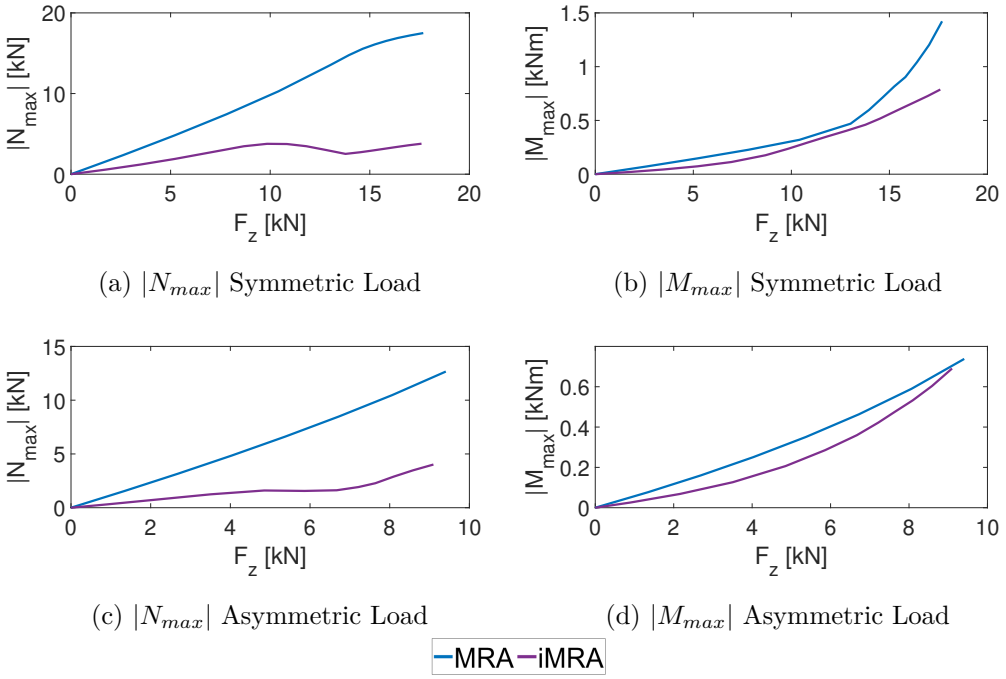


(a) $|N_{max}|$ Symmetric Load

(b) $|M_{max}|$ Symmetric Load

(c) $|N_{max}|$ Asymmetric Load

(d) $|M_{max}|$ Asymmetric Load

Figure 26: Maximum absolute axial force $|N_{max}|$ and bending moment $|M_{max}|$ in the structural elements with $\lambda = 150$ considering to increase the load to perform the GNIA.

## 6. Conclusions

In this paper, a comparative analysis of two form-finding methods with respect to structural stability is provided. The case study is the gridshell that constitutes the roof of the mosque in Dakar, Senegal. The Multibody Rope Approach (MRA) and its enhanced variant, the i-MRA, were used to generate two different structure geometries. A preliminary analysis was performed to establish the differences between the two configurations in the static and dynamic fields as a result of permanent loads. The two structural geometries are then investigated through a linear eigenvalue buckling analysis under two different loading conditions. Three distinct slenderness ratios $\lambda$ of the structural components are considered in the analyses.

The findings of these investigations are used to define the shape of the geometric deviations from the starting geometry. The rescaled first linear buckling mode define the geometry of structural imperfections. An incremental load geometric nonlinear analysis with imperfection (GNIA) is then performed under these conditions.

The outcomes define the equilibrium paths of the investigated structural configurations.

Ultimately, the impacts of material nonlinearity are considered by introducing an elastoplastic constitutive law. Subsequently, the structures are investigated by Geometrically incremental load and Material Nonlinear Imperfection Analyses (GMNIAs).

Different structural behaviours are exhibited by the two geometries. In particular, The MRA case shows the typical behaviour of lowering arches. Both static and instability analyses indicate this behaviour. This structure

shows a structural hierarchy where the central arch works as the main supporting structure.

Conversely, the i-MRA case behaviour resembles a shell structure. In this configuration, no obvious structural hierarchies are observed. The outcome is a more even distribution of stress across the structure.

For the two investigated geometries, two distinct structural behaviours are identified by the equilibrium paths resulting from the GNIA. The MRA case is characterized by a higher elastic buckling load $Q_{EB}$. However, for the MRA geometry $Q_{EB}/Q_{CR} < 1$, which is an indicator of catastrophic postbuckling. On the contrary, in the i-MRA case, postbuckling can be defined as benign being $Q_{EB}/Q_{CR} > 1$. Therefore, even if the peak load $Q_{EB}$ is lower, the i-MRA example exhibits a qualitatively better postbuckling structural behaviour.

The ratios between the elastic buckling load $Q_{EB}$ and the Euler critical load $Q_{CR}$ for the different structural configurations are displayed in Figure 27. It is evident that this ratio is always higher in the i-MRA scenario than it is in the MRA case.

Finally, the GNMIA results demonstrated a reduction in the peak load for the MRA case, obtaining $Q_{EB} > Q_{EP}$. This reduction is due to the stress concentration induced by the MRA geometry. As a result, the yield strength limit is exceeded before the buckling loads are reached.

This phenomenon is not observed in the i-MRA case. The lowering of $Q_{EB}$ resulting from the elastoplastic model introduction is evident in Figure 27 and is limited to the MRA scenario. As a result, the elasto-plastic buckling loads $Q_{EP}$ related to the two geometries are comparable.

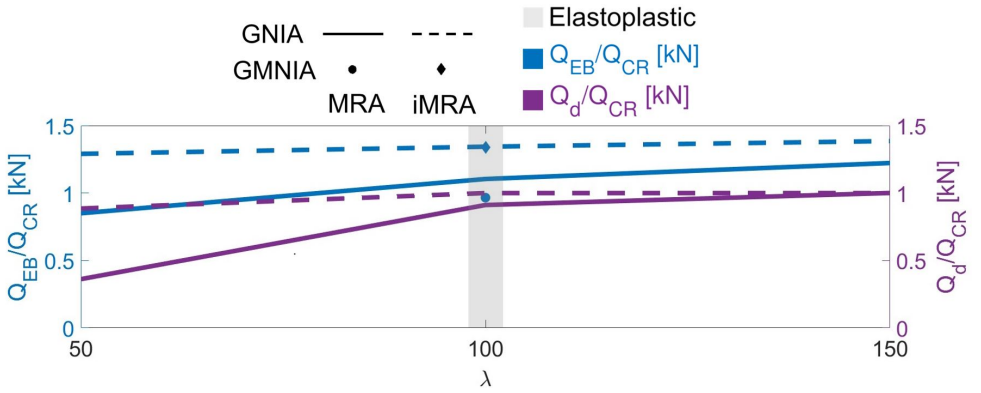


(a) Symmetric load

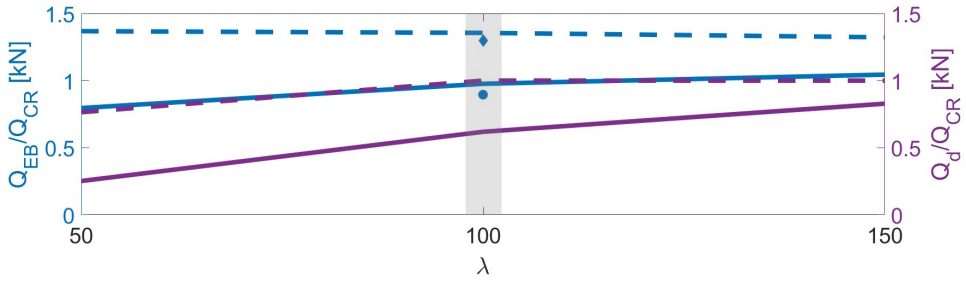


(b) Asymmetric load

Figure 27: Ratios between the elastic buckling load $Q_{EB}$ and the Euler critical load $Q_{CR}$ compared with ratios between design load $Q_d$ and the Euler critical load $Q_{CR}$, for the different structural configurations.

In conclusion, the i-MRA technique enables us to define a structural geometry that is advantageous from a construction perspective. The i-MRA form exhibits superior stress distribution in relation to static loads. Furthermore, a qualitatively better postbuckling behaviour is observed compared to the MRA case. Finally, if the non-linearity of the materials is considered, the peak loads are comparable in the two studied geometries.

## 7. Acknowledgments

The authors would like to express their gratitude to Fragomeli and Partners architectural firm [52] for providing the case study for this research. The authors also acknowledge R. Rivoli for his contribution to the definition of the geometries utilized in this work.

## References

[1] J. Melchiorre, A. Manuello, F. Marmo, S. Adriaenssens, G. Marano, Differential formulation and numerical solution for elastic arches with variable curvature and tapered cross-sections, European Journal of Mechanics-A/Solids 97 (2023) 104757.

[2] I. Liddell, Frei otto and the development of gridshells, Case Studies in Structural Engineering 4 (2015) 39–49.

[3] R. D. Ziemian, Guide to stability design criteria for metal structures, John Wiley & Sons, 2010.

[4] W. IASS, for metal spatial structures,(draft) guide to buckling load evaluation of metal reticulated roof structures, Tech. rep., Tech. Rep. Int Assoc Shell Spatial Struct (2014).

[5] J. W. Hutchinson, J. M. T. Thompson, Imperfections and energy barriers in shell buckling, International Journal of Solids and Structures 148 (2018) 157–168.

[6] H. Fan, W. Gu, L. Li, P. Liu, D. Hu, Buckling design of axially compressed cylindrical shells based on energy barrier approach, International Journal of Structural Stability and Dynamics 21 (12) (2021) 2150165.

[7] R. Groh, A. Pirrera, Probing the stability landscape of cylindrical shells for buckling knockdown factors, Philosophical Transactions of the Royal Society A 381 (2244) (2023) 20220032.

[8] R. M. Jones, Buckling of bars, plates, and shells, Bull Ridge Corporation, 2006.

[9] F. Bazzucchi, A. Manuello, A. Carpinteri, Interaction between different instability phenomena in shallow roofing structures affected by geometrical imperfections, in: Proceedings of IASS Annual Symposia, Vol. 2016, International Association for Shell and Spatial Structures (IASS), 2016, pp. 1–10.

[10] F. Bazzucchi, A. Manuello, A. Carpinteri, Interaction between snap-through and eulerian instability in shallow structures, International Journal of Non-Linear Mechanics 88 (2017) 11–20.

[11] J. Błachut, Locally flattened or dented domes under external pressure, Thin-Walled Structures 97 (2015) 44–52.

[12] D. Wang, M. M. Abdalla, Global and local buckling analysis of grid-stiffened composite panels, Composite Structures 119 (2015) 767–776.

[13] X. Zhao, S. Yan, Y. Chen, Comparison of progressive collapse resistance of single-layer latticed domes under different loadings, Journal of Constructional Steel Research 129 (2017) 204–214.

[14] J. Rondal, D. Dubina, V. Gioncu, Coupled instabilities in metal structures, Springer, 1998.

[15] V. Gioncu, N. Balut, Instability behaviour of single layer reticulated shells, International journal of space structures 7 (4) (1992) 243–252.

[16] V. Gioncu, General theory of coupled instabilities, Thin-Walled Structures 19 (2-4) (1994) 81–127.

[17] J. Thompson, Basic theorems of elastic stability, International Journal of Engineering Science 8 (4) (1970) 307–313.

[18] J. Thompson, Basic principles in the general theory of elastic stability, Journal of the Mechanics and Physics of Solids 11 (1) (1963) 13–20.

[19] J. M. T. Thompson, G. W. Hunt, A general theory of elastic stability, (No Title) (1973).

[20] E. Zeeman, Euler buckling, in: Structural Stability, the Theory of Catastrophes, and Applications in the Sciences: Proceedings of the Conference Held at Battelle Seattle Research Center 1975, Springer, 2006, pp. 373–395.

[21] S. Timoshenko, Buckling of flat curved bars and slightly curved plates (1935).

[22] P. X. Bellini, The concept of snap-buckling illustrated by a simple model, International Journal of Non-Linear Mechanics 7 (6) (1972) 643–650.

[23] H. Rothert, T. Dickel, D. Renner, Snap-through buckling of reticulated space trusses, Journal of the structural division 107 (1) (1981) 129–143.

[24] R. Wiebe, L. Virgin, I. Stanciulescu, S. Spottswood, On snap-through buckling, in: 52nd AIAA/ASME/ASCE/AHS/ASC Structures, Structural Dynamics and Materials Conference 19th AIAA/ASME/AHS Adaptive Structures Conference 13t, 2011, p. 2083.

[25] P. Hao, B. Wang, G. Li, Z. Meng, K. Tian, D. Zeng, X. Tang, Worst multiple perturbation load approach of stiffened shells with and without cutouts for improved knockdown factors, Thin-Walled Structures 82 (2014) 321–330.

[26] H. Wagner, C. Hühne, R. Khakimova, Towards robust knockdown factors for the design of conical shells under axial compression, International Journal of Mechanical Sciences 146 (2018) 60–80.

[27] T. Takeuchi, J. Hajjar, R. Matsui, K. Nishimoto, I. D. Aiken, Local buckling restraint condition for core plates in buckling restrained braces, Journal of constructional steel research 66 (2) (2010) 139–149.

[28] T. Takeuchi, J. Hajjar, R. Matsui, K. Nishimoto, I. Aiken, Effect of local buckling core plate restraint in buckling restrained braces, Engineering Structures 44 (2012) 304–311.

[29] S. Kato, I. Mutoh, M. Shomura, Collapse of semi-rigidly jointed reticulated domes with initial geometric imperfections, Journal of constructional steel research 48 (2-3) (1998) 145–168.

[30] S. Kato, M. Fujimoto, T. Ogawa, Buckling load of steel single-layer reticulated domes of circular plan, Journal of the International Association for Shell and Spatial structures 46 (1) (2005) 41–63.

[31] T. Bulenda, J. Knippers, Stability of grid shells, Computers & Structures 79 (12) (2001) 1161–1174.

[32] T. Von Karman, H.-S. Tsien, The buckling of thin cylindrical shells under axial compression, Journal of the Aeronautical Sciences 8 (8) (1941) 303–312.

[33] J. M. T. Thompson, Advances in shell buckling: theory and experiments, International Journal of Bifurcation and Chaos 25 (01) (2015) 1530001.

[34] Y. Chandra, R. Wiebe, I. Stanciulescu, L. N. Virgin, S. M. Spottswood, T. G. Eason, Characterizing dynamic transitions associated with snap-through of clamped shallow arches, Journal of Sound and Vibration 332 (22) (2013) 5837–5855.

[35] L. Virgin, R. Wiebe, S. Spottswood, T. Eason, Sensitivity in the structural behavior of shallow arches, International Journal of Non-Linear Mechanics 58 (2014) 212–221.

[36] Q. Han, M. Liu, Y. Lu, C. Wang, Progressive collapse analysis of large-span reticulated domes, International Journal of Steel Structures 15 (2015) 261–269.

[37] K. Abedi, G. Parke, Progressive collapse of single-layer braced domes, International Journal of Space Structures 11 (3) (1996) 291–306.

[38] F. Bazzucchi, Snap 'n'roll: Tuning and listening to the progressive buckling of reticulated ensembles, in: Italian Workshop on Shell and Spatial Structures, Springer, 2023, pp. 22–30.

[39] D. Tonelli, N. Pietroni, E. Puppo, M. Froli, P. Cignoni, G. Amendola, R. Scopigno, Stability of statics aware voronoi grid-shells, Engineering Structures 116 (2016) 70–82.

[40] R. Mesnil, C. Douthe, O. Baverel, B. Léger, Linear buckling of quadrangular and kagome gridshells: a comparative assessment, Engineering Structures 132 (2017) 337–348.

[41] F. Fan, J. Yan, Z. Cao, Stability of reticulated shells considering member buckling, Journal of Constructional Steel Research 77 (2012) 32–42.

[42] A. Carpinteri, F. Bazzucchi, A. Manuello, Nonlinear instability analysis of long-span roofing structures: the case-study of porta susa railway-station, Engineering Structures 110 (2016) 48–58.

[43] M. A. Crisfield, A fast incremental/iterative solution procedure that handles "snap-through", in: Computational methods in nonlinear structural and solid mechanics, Elsevier, 1981, pp. 55–62.

[44] M. Bischoff, K.-U. Bletzinger, W. Wall, E. Ramm, Models and finite elements for thin-walled structures, Encyclopedia of computational mechanics (2004).

[45] A. Manuello, J. Melchiorre, L. Sardone, G. C. Marano, Multi-body rope approach for the form-finding of shape optimized grid shell structures, WCCM-APCOM 2022 900 (2022).

[46] A. Manuello Bertetto, J. Melchiorre, G. C. Marano, Improved multi-body rope approach for free-form grid shells, in: Italian Workshop on Shell and Spatial Structures, Springer, 2023, pp. 231–240.

[47] I. Cavaliere, G. Fallacara, A. Manuello Bertetto, J. Melchiorre, G. C. Marano, Multy body rope approach and funicular prototype for a new constructive system for catenary arches, in: Italian Workshop on Shell and Spatial Structures, Springer, 2023, pp. 259–268.

[48] A. Manuello, Multi-body rope approach for grid shells: form-finding and imperfection sensitivity, Engineering Structures 221 (2020) 111029.

[49] A. M. Bertetto, F. Riberi, Form-finding of pierced vaults and digital fabrication of scaled prototype, Curved and Layered Structures 8 (1) (2021) 210–224.

[50] J. Melchiorre, S. Soutiropoulos, A. Manuello Bertetto, G. C. Marano, F. Marmo, Grid-shell multi-step structural optimization with improved multi-body rope approach and multi-objective genetic algorithm, in: Italian Workshop on Shell and Spatial Structures, Springer, 2023, pp. 62–72.

[51] J. Melchiorre, F. Bazzucchi, A. Manuello Bertetto, G. C. Marano, Post-buckling echoes of imra introduced variation in gridshells mechanical behaviour, in: Italian Workshop on Shell and Spatial Structures, Springer, 2023, pp. 379–389.

[52] Fragomeli+Partners, Fragomeli+partners.
URL `https://fragomeliandpartners.com/`

[53] Diana - fea, `https://dianafea.com/`, accessed: 2023-06-03.

[54] L. Co., Lusas modeler reference manual (2008).

[55] M. A. Crisfield, A consistent co-rotational formulation for non-linear, three-dimensional, beam-elements, Computer methods in applied mechanics and engineering 81 (2) (1990) 131–150.

[56] S. Malek, C. Williams, The equilibrium of corrugated plates and shells, Nexus Network Journal 19 (2017) 619–627.